Engineering Fracture Mechanics 320 (2025) 111039

Contents lists available at ScienceDirect

Engineering Fracture Mechanics

journal homepage: www.elsevier.com/locate/engfracmech

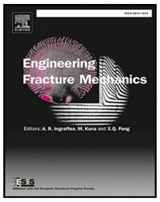

A phase-field study on thermo-mechanical coupled damage evolution and failure mechanisms of sintered silver interconnections

Yanpeng Gong [a,b,*], Yuguo Kou [a], Qiang Yue [b,**], Xiaoying Zhuang [b,c,**], Navid Valizadeh [b], Fei Qin [a], Qiao Wang [d], Timon Rabczuk [e]

[a] *Institute of Electronics Packaging Technology and Reliability, Department of Mechanics, Beijing University of Technology, Beijing, 100124, China*
[b] *Chair of Computational Science and Simulation Technology, Institute of Photonics, Department of Mathematics and Physics, Leibniz University Hannover, 30167 Hannover, Germany*
[c] *Department of Geotechnical Engineering, College of Civil Engineering, Tongji University, Shanghai, 200092, China*
[d] *State Key Laboratory of Water Resources Engineering and Management, Wuhan University, Wuhan, Hubei 430072, China*
[e] *Institute of Structural Mechanics, Bauhaus-Universität Weimar, 99423 Weimar, Germany*

ARTICLE INFO

Keywords:
Sintered silver
Phase-field modeling
Thermomechanical coupling problems
Damage evolution
Failure mechanism

ABSTRACT

Sintered silver paste has emerged as one of the most promising green packaging interconnection materials in electronic packaging due to its combination of low-temperature processing and high-temperature service capabilities. At the microscale, sintered silver exhibits random porous structures influenced by sintering processes, leading to various fracture issues under complex operating conditions, where the mechanical reliability is significantly influenced by thermo-mechanical loading during service. This study establishes a thermo-mechanical coupled phase-field model incorporating mixed tensile–shear failure modes to investigate the mechanical behavior and fracture evolution of random porous structures reconstructed from SEM images of sintered silver. The phase-field approach effectively captures crack initiation and propagation without explicit crack tracking by introducing a regularized description of discontinuities. Numerical predictions of elastic modulus and tensile strength show good agreement with experimental results under various loading conditions, including tensile, shear, and end-notched flexure (ENF) tests. Simulations of crack propagation under thermal and shear loading conditions reveal distinctive crack patterns and complex crack networks. The proposed approach provides an efficient and reliable method for simulating the mechanical behavior and failure mechanisms of sintered silver solder with random porous structures, offering valuable insights for improving electronic package reliability.

1. Introduction

In recent years, the continuous advancement of power electronics technology has driven semiconductor devices toward increased system integration and miniaturization [1]. Third-generation semiconductor devices, particularly Silicon Carbide (SiC) and Gallium

---

* Corresponding author at: Institute of Electronics Packaging Technology and Reliability, Department of Mechanics, Beijing University of Technology, Beijing, 100124, China.
** Corresponding authors.
E-mail addresses: yanpeng.gong@bjut.edu.cn (Y. Gong), qiangyue@iop.uni-hannover.de (Q. Yue), zhuang@iop.uni-hannover.de (X. Zhuang).

https://doi.org/10.1016/j.engfracmech.2025.111039
Received 5 December 2024; Received in revised form 25 February 2025; Accepted 12 March 2025

(a) Paste printing (b) Heat drying

(c) Sintering initiation (d) Final sintered structure

Fig. 1. Schematic illustration of nanosilver particle sintering interconnection mechanism between substrate and chip under pressure-assisted conditions.

Nitride (GaN), have garnered significant attention in electric vehicle and aerospace applications due to their superior properties, including wider bandgap, higher breakdown voltage, lower switching losses, and enhanced thermal conductivity [2]. To ensure reliable operation of these devices under high-temperature and high power density conditions, packaging interconnection materials must demonstrate compatible thermal, electrical, and mechanical properties. Sintered silver paste has emerged as one of the most promising green packaging interconnection materials in electronic packaging, distinguished by its unique combination of low-temperature processing and high-temperature service capabilities. The material consists of nano-sized silver particles/micro-sized silver flakes combined with specific organic components including dispersants, binders, and diluents. When processed at 300 °C, it forms stable interconnections through sintering, resulting in a silver layer characterized by high elastic modulus, excellent electrical and thermal conductivity, and superior fatigue resistance, making it particularly suitable for third-generation power electronic devices [3]. As shown in Fig. 1, the sintering process of nanosilver paste typically comprises four stages: paste printing, heat drying, chip placement, and temperature-elevated sintering. During the paste printing stage (Fig. 1(a)), the nanosilver particles exist in a free state. In the heat drying stage, the organic coating on the nanosilver surface gradually evaporates, leading to particle agglomeration and initial sintering neck formation, resulting in interconnected pores between particles as shown in Fig. 1(b). With further sintering (Fig. 1(c)), the sintering necks between particles grow progressively, particles coarsen, and dense connections form between particles while interconnected pores gradually close. Finally, under pressure assistance, silver particles further grow and coarsen, grain boundaries between particles form continuous networks, and pores between silver particles become rounded and gradually shrink, ultimately forming a sintered silver interconnection layer with random voids as illustrated in Fig. 1(d) [4].

Extensive experimental studies by researchers have demonstrated that sintered silver microstructures exhibit significant variations under different sintering parameters [5]. Wang et al. investigated the porosity and pore size of sintered silver at different sintering times using Scanning Electron Microscopy (SEM), combined with X-ray Diffraction (XRD) measurements and Scherrer equation calculations to track changes in silver particle size over sintering time [6]. Their research revealed that with increased sintering time, both porosity and pore size gradually decrease while average particle size increases. Fan et al. [7] employed the Taguchi orthogonal experimental method to study microstructural changes in sintered silver under various sintering temperatures and holding times. Their findings indicated that relative shrinkage and relative density of sintered silver continuously increase with higher sintering temperatures and longer holding times. Although porosity in sintered silver structures can be modified by adjusting experimental conditions such as sintering temperature and pressure, voids cannot be completely eliminated from the sintered silver layer, significantly affecting the mechanical strength and thermal conductivity of nanosilver joints. From a macroscopic perspective, sintered silver serves both heat dissipation and electrical interconnection functions in power electronic device structures. Under high-temperature environments and applications with mismatched thermal expansion coefficients between layers, residual stresses develop, subjecting the sintered silver layer to various types of fracture issues, thereby affecting the performance reliability of both the silver layer and the entire electronic device. From a microscopic viewpoint, during the sintering process, melting silver particles form networked porous structures. Moreover, sintered silver solder typically operates in harsh environments with complex thermo-electro-mechanical conditions, where internal voids facilitate crack initiation and propagation, leading to device failure [8,9]. Therefore, investigating the fracture behavior of sintered silver holds significant importance for improving electronic device reliability.

Researchers have extensively investigated the influence of porous structures on the mechanical properties of sintered silver through various experimental methods [10,11]. Mechanical characterization studies using tensile tests have revealed that elastic modulus, yield strength, and tensile strength decrease with increasing porosity [11–14]. For instance, Herboth et al. [12] demonstrated through uniaxial tensile tests that specimens with 15% porosity exhibit significantly lower elastic modulus compared to those with 3% porosity. Yu et al. [11] further showed that the tensile strength of sintered silver films decreases with increasing temperature and decreasing strain rate. These experimental findings align well with theoretical predictions based on porous material mechanics [14]. In engineering applications, shear testing methods, particularly lap joint tests, are commonly employed to evaluate the mechanical properties of sintered silver joints. Various studies have investigated the influence of processing parameters on joint strength. Fu et al. [15] utilized Taguchi orthogonal experiments to systematically analyze the effects of sintering temperature, heating rate, and holding time on the average shear strength under pressureless conditions, establishing relationships between sintering parameters and signal-to-noise ratios. Knoerr et al. [16] investigated the influence of sintering pressure on relative density and shear strength at 275 °C for 1 min, revealing that both properties increase progressively with higher sintering pressure. Alternative testing methods have also been explored to characterize the fracture mechanics properties of sintered silver joints, where Li et al. [17] evaluated shear strength using Cu-Ag–Cu lap joint specimens under uniaxial tension, and Zhao et al. [18] investigated Mode II fracture toughness through end-notched flexure (ENF) tests under various sintering conditions, providing comprehensive insights into the mechanical behavior and failure mechanisms of sintered silver joints.

Some researchers have employed numerical simulation approaches to study the mechanical properties of porous sintered silver structures. Carr et al. [19] determined the relationship between porosity and elastic modulus using finite element analysis based on 3D structures obtained through scanning electron microscopy. Chen et al. [20] reconstructed the actual 3D microstructure of sintered films using focused ion beam (FIB) scanning electron microscope tomography, and calculated elastic modulus through finite element modeling, achieving good agreement with experimental results. To explore the influence of microstructural features beyond porosity, they employed cellular automata methods to numerically analyze both real microstructures and artificial microstructures based on spherical mono-sized particles at constant porosity. Yao et al. [21] investigated the tensile strength of nanoporous silver through experiments and molecular dynamics analysis, studying the effects of sintering temperature on porosity and ultimate strength, and simulated sintered silver structures with cubic, helical, and spherical pores. Su et al. [22] pioneered the use of one-cut Gaussian random field model for modeling porous structures of sintered silver, followed by fracture simulation using a thermo-elastic–plastic phase-field model. Long et al. [23] attempted to investigate the influence of sintered silver's microstructure on its fracture behavior using crystal plasticity finite element methods.

Based on the above review, the microstructure of sintered silver significantly influences the mechanical properties of sintered silver joints. Under complex mechanical and thermal conditions, sintered nanosilver paste exhibits cracks of varying shapes and sizes between pores. However, current research on the mechanism of microstructural effects on the fracture mechanics properties of sintered silver remains incomplete. The phase-field model employed by Su et al. [22] only considered the effect of tensile stress on computational results, neglecting the damage induced by shear stress or combined tensile–shear stress in porous sintered silver structures. Pillai et al. [24] proposed a phase-field model for predicting crack evolution in heterogeneous solids and porous materials, qualitatively simulating crack propagation in both pure solids and porous materials. Their comparative study of crack propagation behavior in homogeneous and heterogeneous materials revealed significant path deviation when material heterogeneity was considered. However, their research was based on a macroscopic scale without considering microstructural details. Generally, the pore diameter in sintered silver exceeds half the crack length, and the thickness of the sintered silver solder layer is relatively small at the macroscopic scale. Therefore, microscopic phase-field modeling of porous sintered silver materials must consider the characteristics of random voids. Dittmann et al. [25] introduced a framework to simulate ductile fracture in porous thermo-elasto-plastic solids under large deformation conditions, investigating the effects of microvoid nucleation, growth, and coalescence on final fracture at the macroscopic scale. While their approach incorporated microstructural effects through void volume fraction homogenization, this simplification may not adequately capture the complex fracture behavior in sintered silver solder layers. With characteristic dimensions of 0.02-0.05 μm and pore diameters larger than half the crack length, the crack evolution process is intrinsically linked to local microstructural features, necessitating explicit consideration of microstructural effects on macroscopic mechanical response.

During operation of power devices, sintered silver solder experiences thermal stresses under high temperature environments and mismatched thermal expansion coefficients between layers, leading to various types of fracture issues. However, microscale studies of these complex failure modes are currently lacking. Therefore, to analyze such porous materials, this work proposes a thermo-mechanical phase-field model considering mixed tensile–shear failure modes to simulate the mechanical behavior and crack evolution in microporous structures. The phase-field fracture approach diffuses cracks within a finite-width local band by introducing an intrinsic length scale, enabling direct calculation of crack development during the solution of phase field equations without requiring additional criteria for crack tip tracking. The phase-field method has been widely applied to study crack propagation in various materials, including concrete [26–30], multiphase materials [31], piezoelectric materials [32], and functionally graded materials [33]. It has also been extended to simulate mechanical behavior and crack propagation in solids under multiple physical conditions, such as elastoplasticity [34], thermoelasticity [35–37], thermo-elastoplasticity [38], electronic packaging [35], and chemical thermodynamics [39]. In [40], a variation-energy-based physics-informed neural network (PINN) for phase-field fracture modeling is proposed, which offers improved computational efficiency and more accurate crack path predictions compared to conventional residual-based PINN approaches. Therefore, phase-field method is particularly suitable for simulating fracture processes in porous sintered silver structures under complex working conditions.

This work aims to establish a thermo-elastic phase-field model for sintered silver materials with random microporous structures, considering mixed tensile–shear failure modes. The remainder of this paper is organized as follows. Section 2 presents the theory of thermo-mechanical coupled phase-field fracture model considering mixed tensile–shear failure modes. Section 3 describes the modeling procedure for sintered silver structures. Section 4 presents numerical simulations of failure behavior under tensile and shear loading, along with ENF test simulations, and analyzes crack propagation processes under thermal loading and chip shear conditions in power modules. Finally, Section 5 summarizes the main conclusions of this study.

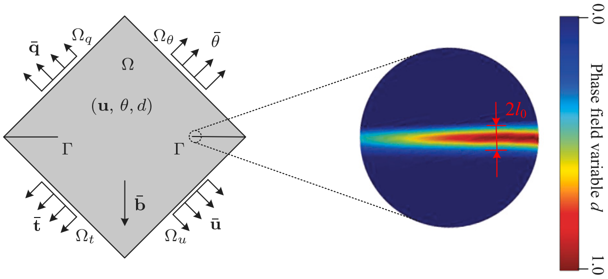

Fig. 2. Embedded cracks in solids and their phase-field regularization. The boundary satisfy: $\partial\Omega_u \cap \partial\Omega_t = \emptyset$, $\partial\Omega_u \cup \partial\Omega_t = \partial\Omega$, $\partial\Omega_\theta \cap \partial\Omega_q = \emptyset$ and $\partial\Omega_\theta \cup \partial\Omega_q = \partial\Omega$.

2. Phase-field fracture model

2.1. Crack diffusion

In the phase-field model, crack regularization in the local region is achieved through a phase field variable d and its gradient ∇d, where the material failure process is represented by the evolution of the phase field. During the solution process of the phase field governing equations, the crack development state can be directly obtained without additional criteria for crack tip tracking, making it particularly suitable for analyzing complex fracture processes in sintered silver materials.

For an arbitrary domain $\Omega \subset \mathbb{R}^D$ containing a crack Γ, as shown in Fig. 2, there are 3 independent variables in the domain: displacement field $\mathbf{u}$, temperature θ, and phase-field variable d. The boundary conditions satisfy the following relationships: displacement boundary condition $\mathbf{u} = \bar{\mathbf{u}}$ on Γ_u, traction boundary condition $\mathbf{t} = \bar{\mathbf{t}}$ on Γ_t, temperature boundary condition $\theta = \bar{\theta}$ on Γ_θ, and heat flux boundary condition $\mathbf{q} = \bar{\mathbf{q}}$ on Γ_q. On the internal crack Γ, the phase-field variable d characterizes the degree of damage at a certain position in the solid, where $d = 0$ indicates the material is intact, $d = 1$ indicates complete fracture has occurred, and $0 < d < 1$ represents partial damage. Here, $\bar{\mathbf{u}}$, $\bar{\mathbf{t}}$, $\bar{\theta}$, and $\bar{\mathbf{q}}$ represent the prescribed displacement, prescribed surface traction, prescribed temperature, and prescribed heat flux, respectively.

The crack Γ is regularized by introducing a crack surface density function $\gamma(d, \nabla d)$, where the regularization parameter l_0 represents the internal length scale of the diffuse crack interface. When l_0 approaches zero, the diffuse interface converges to a sharp crack representation. This regularization can be expressed mathematically as:

$$\Gamma = \int_\Omega \gamma(d, \nabla d)\ \mathrm{d}\Omega = \frac{1}{c_0 l_0} \int_\Omega \left(\alpha(d) + l_0^2 |\nabla d|^2\right)\ \mathrm{d}\Omega \tag{1}$$

$c_0 = 4\int_0^1 \sqrt{\alpha(\vartheta)}\mathrm{d}\vartheta$ is a normalization constant that ensures the equivalence between the sharp and diffuse crack descriptions; $\alpha(d)$ is a geometric function of the crack. The present work adopts the form derived from the unified phase-field model proposed by Wu et al. [41], where $\alpha(d) = 2d - d^2$ and $c_0 = \pi$.

Based on the crack surface density function and normalization constant c_0, a coupled multi-physics model is developed that encompasses three primary processes: thermal, mechanical, and fracture processes. The model accounts for the multi-field interactions within the thermoelastic body,specifically addressing two key aspects: (1) the interaction between phase-field fracture and displacement fields, and (2) the degradation of thermal conductivity near cracks through the phase-field degradation function.

2.2. Governing equations

In the framework of fracture mechanics, the energy functional for damage simulation Π consists of three components: bulk energy Ψ_b, crack surface energy Ψ_s, and external work W_{ext}. This can be expressed as

$$\Pi = \Psi_b + \Psi_s - W_{ext} \tag{2}$$

The complete form of the energy functional is

$$\Pi(\mathbf{u}, d) = \int_\Omega \psi_b(\varepsilon, d)\ \mathrm{d}\Omega + \int_\Omega \gamma(d, \nabla d)\ \mathrm{d}\Omega - W_{ext} \tag{3}$$

In phase-field modeling, the diffuse crack representation requires modification of the bulk energy through a degradation function. The modified bulk energy takes the form

$$\Psi_b = \int_\Omega \psi_b(\varepsilon(\mathbf{u}), d)\ \mathrm{d}\Omega = \int_\Omega \omega(d)\psi_0(\varepsilon(\mathbf{u}))\ \mathrm{d}\Omega \tag{4}$$

The elastic strain energy density ψ_0 is defined as:

$$\psi_0 = \frac{1}{2}\lambda \mathrm{tr}^2[\varepsilon] + \mu \mathrm{tr}[\varepsilon^2] \tag{5}$$

where λ and μ are Lamé constants, $\omega(d)$ is the degradation function governed by the phase-field variable d, $\boldsymbol{\varepsilon}(\mathbf{u})$ is the strain tensor dependent on displacement field $\mathbf{u}$. The components of strain tensor $\boldsymbol{\varepsilon}$ can be expressed as

$$\boldsymbol{\varepsilon} = \frac{1}{2}\left[\nabla^{\mathrm{T}}\mathbf{u} + \nabla\mathbf{u}\right] \tag{6}$$

In the unified phase-field theory proposed by Wu et al. [41], the degradation function is given by

$$\omega(d) = \frac{(1-d)^p}{(1-d)^p + S(d)} = \frac{1}{1+\phi(d)}, \quad \phi(d) = \frac{S(d)}{(1-d)^p} \tag{7}$$

where $p > 0$, $S(d) > 0$, and $S(d)$ is defined as

$$S(d) = a_1 d + a_1 a_2 d^2 + a_1 a_2 a_3 d^3 + a_1 a_2 a_3 a_4 d^3 + \cdots = a_1 d + a_1 b_2 d^2 + a_1 b_3 d^3 + a_1 b_4 d^3 + \cdots \tag{8}$$

with $b_m = \prod_{n=2}^{m} a_n$ representing coefficients calibrated through standard material properties. Here, $\phi(d)$ is a function that relates to the degradation of material properties. When $d = 0$ (undamaged state), we have $\phi(0) = S(0) = 0$, and consequently $\omega(0) = 1$, indicating full material integrity.

For different softening curves, the coefficients $a_i (i = 1, 2, 3, \ldots)$ can be expressed in a uniform form as follows

$$a_1 = \frac{4}{c_0 l_0}\frac{E G_c}{f_t^2} \tag{9}$$

$$a_2 = \frac{1}{2}[(-\frac{16\pi}{c_0}\frac{G_c}{f_t^2}k_0)^{\frac{2}{3}} + 1] - (p+1) \tag{10}$$

$$a_3 = \begin{cases} 0 & p > 2 \\ \frac{1}{a_2}[\frac{1}{2}(\frac{c_0 w_c f_t}{2\pi G_c})^2 - (1+a_2)] & p = 2 \end{cases} \tag{11}$$

where $k_0 < 0$ is the initial slope of the selected softening curve, w_c is the final crack opening displacement at complete failure, and f_t is the material's tensile strength. While higher-order polynomials $S(d)$ can provide more accurate results at increased computational cost, this paper adopts a quadratic form with $a_i (i \geq 3) = 0$ for simplicity.

The initial slope and final crack opening of the selected softening curve can be calculated as:

$$k_0 = -\frac{c_0}{16\pi}\frac{f_t^2}{G_c}[2(a_2 + p + 1) - 1]^{3/2} \tag{12}$$

$$w_c = \frac{2\pi G_c}{c_0 f_t}\sqrt{2S(1)}\lim_{d^* \to 1}(1-d^*)^{1-p/2} \tag{13}$$

where $S(1) = a_1(1 + b_2 + b_3 + \cdots)$ is the value of polynomial $S(d)$ at $d = 1$.

For the linear softening model used in this paper, the parameters reduce to:

$$k_0 = -\frac{f_t^2}{2G_c}, \quad w_c = \frac{2G_c}{f_t}, \quad p = 2 \quad \Rightarrow \quad a_2 = -\frac{1}{2}, \quad a_3 = 0 \tag{14}$$

The expression for external work is given by

$$W_{ext} = \int_{\Omega} \bar{\mathbf{b}} \cdot \mathbf{u} \, \mathrm{d}\Omega + \int_{\partial\Omega_t} \bar{\mathbf{t}} \cdot \mathbf{u} \, \mathrm{d}\Omega \tag{15}$$

where $\bar{\mathbf{b}}$ is the body force and $\partial\Omega_t$ represents the traction boundary.

Considering the diffuse crack treatment, the crack surface energy can be approximated as the product of the critical energy release rate G_c and the crack surface

$$\Psi_s = G_c \int_{\Gamma} \mathrm{d}\Gamma \approx G_c \int_{\Omega} \gamma(d, \nabla d)\mathrm{d}\Omega \tag{16}$$

where Γ represents the crack surface, and $\gamma(d, \nabla d)$ is the crack surface density function.

The strain energy density function is decomposed using two distinct degradation functions to capture both tensile and shear damage modes:

$$\psi_0 = \omega_I(d)\psi_{0I}^{+} + \omega_{II}(d)\psi_{0II}^{+} + \psi_0^{-} \tag{17}$$

where ψ_{0I}^{+} represents the tensile strain energy density due to normal stress; ψ_{0II}^{+} represents the shear strain energy density due to tangential stress; ψ_0^{-} represents the remaining strain energy; ω_I and ω_{II} are the degradation functions for tensile and shear energies, respectively.

For plane stress conditions, these energy components are computed as:

$$\psi_{0I}^{+} = \begin{cases} \frac{(\bar{\sigma}^{rr})^2}{2E} & \text{if } \bar{\sigma}^{rr} > 0 \\ 0 & \text{if } \bar{\sigma}^{rr} \leq 0 \end{cases} \tag{18}$$

$$\psi_{0II}^{+} = \begin{cases} \frac{(\bar{\sigma}^{rm})^2}{2\mu} = \frac{\bar{\tau}^2}{2\mu} & \text{if } \bar{\sigma}_1 > 0 \\ 0 & \text{if } \bar{\sigma}_1 \leq 0 \end{cases} \tag{19}$$

$$\psi_0^{-} = \psi_0 - \psi_{0I}^{+} - \psi_{0II}^{+} \tag{20}$$

The effective stresses are related to the actual stresses through

$$\begin{bmatrix} \bar{\sigma}^{rr} \\ \bar{\sigma}^{mm} \\ \bar{\sigma}^{rm} \end{bmatrix} = \begin{bmatrix} \frac{1}{\omega_I(d)} & 0 & 0 \\ 0 & \frac{1}{\omega_I(d)} & 0 \\ 0 & 0 & \frac{1}{\omega_{II}(d)} \end{bmatrix} \begin{bmatrix} \sigma^{rr} \\ \sigma^{mm} \\ \sigma^{rm} \end{bmatrix} \tag{21}$$

The degradation functions take the form:

$$\omega_I = \frac{1}{1 + \phi_I(d)} \tag{22}$$

$$\omega_{II} = \frac{1}{1 + \phi_{II}(d)} \tag{23}$$

where r and m denote the unit normal and tangential vectors, respectively.

According to Ref. [42,43], through fracture analysis of a 2D rod, the crack evolution equation under tensile–shear failure mode is obtained

$$\omega_I'(d)\frac{\psi_{0I}^{+}}{G_{cI}} + \omega_{II}'(d)\frac{\psi_{0II}^{+}}{G_{cII}} \geq \frac{2l_0^2\nabla^2 d - \alpha'(d)}{c_0 l_0} \tag{24}$$

where G_{cI} is the fracture toughness for pure tensile failure; G_{cII} is the fracture toughness for pure shear failure; $\omega_I'(d)$ is the derivative of degradation function for mode I; $\omega_{II}'(d)$ is the derivative of degradation function for mode II; ψ_{0I}^{+} is the positive part of elastic energy for mode I; ψ_{0II}^{+} is the positive part of elastic energy for mode II; $\alpha'(d)$ is the derivative of the geometric function; $\nabla^2 d$ is the Laplacian of the phase-field variable. The fracture toughness for mode I (tensile failure) and II (shear failure) are given by

$$G_{cI} = \frac{c_0 l_0}{2E}\frac{\phi'(0)}{\alpha'(0)} f_t^2 \tag{25}$$

$$G_{cII} = \frac{\chi^2 E}{\mu} G_{cI} \tag{26}$$

where E is the elastic modules; f_t is the tensile strength; χ is the ratio between the critical shear strength τ_s and the critical tensile strength f_t. The term $\phi'(0)$ represents the derivative of $\phi(d)$ (given in Eq. (7)) evaluated at $d = 0$. For more detailed information about this formulation, please refer to Ref. [42].

The phase-field model used in this work can indeed transition between tensile, shear, and mixed-mode tensile–shear damage, governed by the parameter χ. Based on the unified fracture criterion proposed by Zhang et al. [44], different fracture modes emerge depending on material properties, even under identical geometric and loading conditions. In this mixed-mode phase field model, we introduce a unified damage criterion represented by the elliptic equation

$$\frac{\bar{\sigma}^2}{\sigma_t^2} + \frac{\bar{\tau}^2}{\tau_s^2} = 1 \tag{27}$$

where σ_t and τ_s represent the critical tensile and shear damage stresses, respectively. Material damage initiates when the effective tensile stress $\bar{\sigma}$ and shear stress $\bar{\tau}$ satisfy this criterion.

The ratio $\chi = \tau_s/\sigma_t$ determines the dominant fracture mode, reproducing four classical damage criteria

$$\chi = \frac{\tau_s}{\sigma_t} = \begin{cases} 0 & \text{Tresca criterion} \\ > \frac{\sqrt{2}}{2} & \text{Maximum normal stress criterion} \\ < \frac{\sqrt{2}}{2} & \text{Mohr–Coulomb criterion} \\ \frac{\sqrt{3}}{3} & \text{von Mises criterion} \end{cases} \tag{28}$$

This unified framework enables analysis of multiple fracture modes: (1) Type I fracture ($\chi > \sqrt{2}/2$); (2) Type II fracture ($\chi = 0$), and (3) Mixed Type I + II fracture ($0 < \chi < \sqrt{2}/2$). Further details of this unified criterion can be found in [42].

The governing equations for the phase-field model considering mixed tensile–shear failure modes are

$$\begin{cases} \operatorname{div}\boldsymbol{\sigma}(\mathbf{u}, d) + \bar{\mathbf{b}} = \mathbf{0} & \text{in } \Omega \\ \omega'(d)\mathcal{H} \geq \frac{2l_0^2\nabla^2 d - \alpha'(d)}{c_0 l_0} & \text{in } \Theta \end{cases} \tag{29}$$

where $\boldsymbol{\sigma}$ is the degraded Cauchy stress tensor, and $\mathcal{H}$ is a history field introduced to prevent crack healing:

$$\mathcal{H}(\mathbf{x}, t) = \max(\bar{Y}_0, \max_{t\in[0,T]} \bar{Y}_t) \tag{30}$$

where $\mathbf{x}$ is the spatial position, t is the current time, and T is the total time period. $\bar{Y}_0$ represents the magnitude of history field variable required for material damage initiation, and $\bar{Y}_t$ denotes the tensile strain energy obtained at the tth load step. This work introduces two history field variables for tensile stress $\mathcal{H}_I$ and shear stress $\mathcal{H}_{II}$, respectively, to address the irreversibility of damage evolution during the tensile–shear failure process. Furthermore, to address the sensitivity issue of the phase-field model to the internal length scale l_0, this method adopts the concept from PF-CZM and establishes a similar form of history field. Consequently, in the definition of history field, $\bar{Y}_0$ and $\bar{Y}_t$ take the following forms:

$$\bar{Y}_0 = \frac{\alpha'(0)}{c_0 l_0 \phi'(0)}, \ \bar{Y}_t = \mathcal{H}_I + \mathcal{H}_{II} \tag{31}$$

and

$$\mathcal{H}_I = \frac{\psi^+_{0I}(t)}{G_{cI}}, \ \mathcal{H}_{II} = \frac{\psi^+_{0II}(t)}{G_{cII}} \tag{32}$$

where $\psi^+_{0I}(t)$, $\psi^+_{0II}(t)$ are positive parts of mode I and II elastic energies.

In the actual computation process, the phase-field model can also be viewed as a multi-field coupling problem between displacement field and phase field. Thus, the governing equations and boundary conditions of the phase-field model can be rewritten in a similar form

$$\begin{cases} \nabla\cdot\boldsymbol{\sigma} + \bar{\mathbf{b}} = \mathbf{0} & \text{in} \quad \Omega \\ \boldsymbol{\sigma}\cdot\mathbf{n} = \bar{\mathbf{t}} & \text{on} \quad \partial\Omega \end{cases} \tag{33}$$

and

$$\begin{cases} \nabla\cdot\mathbf{g} + \mathbf{Q}(d) = \mathbf{0} & \text{in} \quad \Theta \\ \mathbf{g}\cdot\mathbf{n}_\Theta \geq 0 & \text{on} \quad \partial\Theta \end{cases} \tag{34}$$

where $\mathbf{n}$ is the outward normal vector at any external boundary of the domain, and $\mathbf{n}_\Theta$ is the outward normal vector of the diffuse damage zone. The flux vector $\mathbf{g}$ and source term $\mathbf{Q}(d)$ are respectively defined as

$$\begin{cases} \mathbf{g} = \frac{2l_0}{c_0}\nabla d \\ \mathbf{Q}(d) = -\omega'(d)\mathcal{H} - \frac{1}{c_0 l_0}\alpha'(d) \end{cases} \tag{35}$$

Eq. (33) is the equation for solving the displacement field problem, and Eq. (34) is the crack evolution equation for solving the phase field problem. Note that Eqs. (33) and (34) are formulated without incorporating thermal effects.

In this work, the total strain $\boldsymbol{\varepsilon}_t$ is decomposed into elastic strain $\boldsymbol{\varepsilon}_e$ and thermal strain $\boldsymbol{\varepsilon}_\theta$, i.e.,

$$\boldsymbol{\varepsilon}_t = \boldsymbol{\varepsilon}_e + \boldsymbol{\varepsilon}_\theta \tag{36}$$

The thermal strain $\boldsymbol{\varepsilon}^\theta = \alpha_0 \Delta\theta \mathbf{I}$, where α_0 is the linear thermal expansion coefficient, $\mathbf{I}$ is the identity tensor, and $\Delta\theta = \theta - \theta_0$ is the temperature increment from the initial reference temperature θ_0. Assuming the heat conduction process follows Fourier's law, the heat flux $\mathbf{q}$ is given by

$$\mathbf{q}(\mathbf{u}, d, \theta) = -\mathbf{g}(d) k_0 \nabla\theta \tag{37}$$

where k_0 is the thermal conductivity of the uncracked material, and the degradation function $\mathbf{g}(d)$ ensures that no heat flow crosses the crack when it opens. In this work, a general form of degradation function is adopted $\mathbf{g}(d) = \omega(d)$. This degradation function is controlled by the phase field variable d, where $d = 0$ represents the undamaged material with full thermal conductivity, and $d = 1$ indicates complete damage with zero thermal conductivity. While heat transfer can indeed occur across cracks in practical situations, the precise physics of heat transfer in cracked media remains an active area of research. Our current approach adopts a simplified model where the thermal conductivity degradation is controlled by the phase field variable through the uniform degradation function $\mathbf{g}(d) = \omega(d)$, reducing to zero when $d = 1$. We acknowledge that alternative, more sophisticated approaches exist: Svolos et al. developed analytical homogenization methods for calculating effective thermal conductivity [45]; and Dittmann et al. proposed crack-opening-dependent thermal degradation functions [46]. However, we chose our current formulation to balance physical representation with computational efficiency. While this simplification may not capture all aspects of near-crack heat transfer, it provides a tractable framework for our initial investigation [35]. In addition, although Eq. (37) appears to suggest that heat transfer is inhibited under all crack deformation modes, our model specifically considers crack formation only under tensile–shear mixed-mode loading conditions, explicitly excluding compressive crack scenarios. Thus, the apparent limitation of heat transfer under compression does not manifest in our simulations, as crack formation is restricted to mixed-mode loading only.

The governing equations for the thermo-mechanical-damage coupled problem can be written as

$$\begin{cases} \nabla\cdot\boldsymbol{\sigma} + \overline{\mathbf{b}} = \mathbf{0} & \text{in} \quad \Omega \\ \rho c_\theta \dot{\theta} + \nabla\cdot\mathbf{q} = \bar{\gamma} & \text{in} \quad \Omega \\ \nabla\cdot\mathbf{g} + \mathbf{Q}(d) = \mathbf{0} & \text{in} \quad \Theta \end{cases} \tag{38}$$

and the boundary conditions are

$$\begin{cases} \sigma \cdot \mathbf{n} = \bar{\mathbf{t}} & \text{on} \quad \partial\Omega_t \\ \mathbf{q} \cdot \mathbf{n} = \bar{\mathbf{q}} & \text{on} \quad \partial\Omega_q \\ \mathbf{g} \cdot \mathbf{n}_\Theta \geq 0 & \text{on} \quad \partial\Theta \end{cases} \tag{39}$$

where ρ is the density, c_θ is the specific heat capacity, $\dot{\theta}$ is the time derivative of temperature, and $\bar{\gamma}$ is the heat source term. In the proposed thermo-mechanical coupled phase-field model, nine material properties need to be obtained in advance as input parameters for computation. They are: elastic modulus E, Poisson's ratio ν, tensile strength f_t, fracture toughness G_c, mass density ρ, thermal conductivity coefficient k_0, specific heat capacity c_θ, linear thermal expansion coefficient α_0, and critical shear-tension ratio χ.

2.3. Numerical discretization using finite element method

To implement the phase-field method for solving thermo-mechanical coupled problems, a discretization scheme is proposed using user subroutines in Abaqus to discretize the governing equations and implement the phase-field method. The displacement $\mathbf{u}$, temperature θ, and damage d in finite elements are discretized. The discretized form with linear shape functions can be approximated as

$$\begin{aligned} \mathbf{u}(\mathbf{x},t) &= \sum_{i=1}^{n_e} \mathbf{N}_i^u(\mathbf{x})\mathbf{u}_i(t) = \mathbf{N}_u\tilde{\mathbf{u}} \\ \theta(\mathbf{x},t) &= \sum_{i=1}^{n_e} N_i^\theta(\mathbf{x})\theta_i(t) = \mathbf{N}_\theta\tilde{\theta} \\ d(\mathbf{x},t) &= \sum_{i=1}^{n_e} N_i^d(\mathbf{x})d_i(t) = \mathbf{N}_d\tilde{\mathbf{d}} \end{aligned} \tag{40}$$

where $\mathbf{u}_i(t)$, $\theta_i(t)$, and $d_i(t)$ represent the nodal values at the ith node at time t, n_e is the number of nodes per element, $\mathbf{x}$ (x_1, x_2) denotes the spatial coordinates, the nodal values are collected into lumped vectors $\tilde{\mathbf{u}}$, $\tilde{\theta}$ and $\tilde{\mathbf{d}}$. The shape functions $\mathbf{N}_i^u(\mathbf{x})$, $N_i^\theta(\mathbf{x})$, and $N_i^d(\mathbf{x})$ are used to interpolate displacement, temperature, and damage fields respectively, where the displacement shape function is a matrix defined as

$$\mathbf{N}_i^u(\mathbf{x}) = \begin{bmatrix} N_i^u(\mathbf{x}) & 0 \\ 0 & N_i^u(\mathbf{x}) \end{bmatrix},$$

These shape functions are assembled into matrices for each field

$$\mathbf{N}_u = \begin{bmatrix} \mathbf{N}_1^u & \mathbf{N}_2^u & \cdots & \mathbf{N}_{n_e}^u \end{bmatrix},\ \mathbf{N}_\theta = \begin{bmatrix} N_1^\theta & N_2^\theta & \cdots & N_{n_e}^\theta \end{bmatrix},\ \mathbf{N}_d = \begin{bmatrix} N_1^d & N_2^d & \cdots & N_{n_e}^d \end{bmatrix}.$$

The discretized forms of the strain tensor and the gradients of temperature and phase fields are obtained by differentiating the shape functions

$$\begin{aligned} \varepsilon(\mathbf{x},t) &= \sum_{i=1}^{n_e} \mathbf{B}_i^u(\mathbf{x})\mathbf{u}_i(t) = \mathbf{B}_u\tilde{\mathbf{u}} \\ \nabla\theta(\mathbf{x},t) &= \sum_{i=1}^{n_e} \mathbf{B}_i^\theta(\mathbf{x})\theta_i(t) = \mathbf{B}_\theta\tilde{\theta} \\ \nabla d(\mathbf{x},t) &= \sum_{i=1}^{n_e} \mathbf{B}_i^d(\mathbf{x})d_i(t) = \mathbf{B}_d\tilde{\mathbf{d}} \end{aligned} \tag{41}$$

Matrices $\mathbf{B}_i^u(\mathbf{x})$, $\mathbf{B}_i^\theta(\mathbf{x})$, and $\mathbf{B}_i^d(\mathbf{x})$ contain derivatives of the shape functions for displacement, temperature, and phase fields, respectively. These matrices take the following forms

$$\mathbf{B}_i^u(\mathbf{x}) = \begin{bmatrix} \partial_x N_i^u & 0 \\ 0 & \partial_y N_i^u \\ \partial_y N_i^u & \partial_x N_i^u \end{bmatrix},\ \mathbf{B}_i^\theta(\mathbf{x}) = \begin{bmatrix} \partial_x N_i^\theta \\ \partial_y N_i^\theta \end{bmatrix},\ \mathbf{B}_i^d(\mathbf{x}) = \begin{bmatrix} \partial_x N_i^d \\ \partial_y N_i^d \end{bmatrix}.$$

The derivatives of the shape functions are assembled into matrices for each field

$$\mathbf{B}_u = [\mathbf{B}_1^u \quad \mathbf{B}_2^u \quad \cdots \quad \mathbf{B}_{n_e}^u],\ \mathbf{B}_\theta = [\mathbf{B}_1^\theta \quad \mathbf{B}_2^\theta \quad \cdots \quad \mathbf{B}_{n_e}^\theta],\ \mathbf{B}_d = [\mathbf{B}_1^d \quad \mathbf{B}_2^d \quad \cdots \quad \mathbf{B}_{n_e}^d].$$

The residual vectors for displacement, temperature, and damage are

$$\mathbf{r}_u := \mathbf{f}_u^{\text{ext}} - \int_\Omega \mathbf{B}_u^{\text{T}}\sigma \mathrm{d}\Omega = \mathbf{0} \tag{42}$$

$$\mathbf{r}_\theta := \mathbf{f}_\theta^{\text{ext}} + \int_\Omega \mathbf{B}_\theta^{\text{T}}\mathbf{q}\mathrm{d}\Omega - \mathbf{C}\dot{\tilde{\theta}} = \mathbf{0} \tag{43}$$

$$\mathbf{r}_d := \int_\Omega \mathbf{N}_d^{\mathrm{T}} \mathbf{Q} \mathrm{d}V - \int_\Theta \mathbf{B}_d^{\mathrm{T}} \mathbf{g} \mathrm{d}V = \mathbf{0} \tag{44}$$

in which $\mathbf{f}_u^{\mathrm{ext}}$ and $\mathbf{f}_\theta^{\mathrm{ext}}$ are the external force vector and heat flux vector acting on the system and can be expressed as

$$\mathbf{f}_u^{\mathrm{ext}} = \int_\Omega \mathbf{N}_u^{\mathrm{T}} \bar{\mathbf{b}} \mathrm{d}\Omega + \int_{\partial\Omega} \mathbf{N}_u^{\mathrm{T}} \bar{\mathbf{t}} \mathrm{d}\Gamma$$

and

$$\mathbf{f}_\theta^{\mathrm{ext}} = \int_\Omega \mathbf{N}_\theta^{\mathrm{T}} \bar{\gamma} \mathrm{d}\Omega - \int_{\partial\Omega_q} \mathbf{N}_\theta^{\mathrm{T}} \bar{\mathbf{q}} \mathrm{d}\Gamma$$

and $\mathbf{C}$ is the heat capacity matrix, which can be obtained from

$$\mathbf{C} = \int_\Omega \rho c_\theta \mathbf{N}_\theta^{\mathrm{T}} \mathbf{N}_\theta \mathrm{d}\Omega \tag{45}$$

and $\dot{\tilde{\boldsymbol{\theta}}} = \mathrm{d}\tilde{\boldsymbol{\theta}}/\mathrm{d}t$ is the rate of change of nodal temperatures.

Due to the nonlinear nature of the thermo-mechanical-damage coupled system of equations, a staggered iteration algorithm is implemented in solving the governing equations to enhance numerical convergence. The solution strategy involves decomposing the governing equations into two subproblems: the thermo-mechanical coupled subproblem and the damage evolution subproblem. These subproblems are solved alternately through a fixed-point iteration scheme. The solution procedure consists of two main steps: (1) Solve for displacement and temperature fields $(\tilde{\mathbf{u}}, \tilde{\boldsymbol{\theta}})$ while keeping the phase field fixed; (2) Update the phase field d using the computed displacement and temperature fields: (a) If convergence criteria are met, advance to next time increment; (b) If not converged, repeat the iteration process.

For the time discretization, let $\mathbf{R}_n$ and $\mathbf{z}_n$ represent the known residual and quantity values $(\tilde{\mathbf{u}}_n, \tilde{\boldsymbol{\theta}}_n, \tilde{\mathbf{d}}_n)$ at the current time step t_n, with Δt denoting the time increment and $\Delta t = t_{n+1} - t_n$. Since only temperature field involves time derivatives, adopting the implicit backward Euler time integration method to approximate the time derivative

$$\dot{\tilde{\boldsymbol{\theta}}} \approx \frac{\tilde{\boldsymbol{\theta}}_{n+1} - \tilde{\boldsymbol{\theta}}_n}{\Delta t} \tag{46}$$

The temperature field residual is expressed as

$$\mathbf{r}_\theta = \Delta t\, \mathbf{f}_{\theta,n+1}^{\mathrm{ext}} + \Delta t \int_\Omega \mathbf{B}_\theta^T \mathbf{q} \mathrm{d}\Omega - \mathbf{C}(\tilde{\boldsymbol{\theta}}_{n+1} - \tilde{\boldsymbol{\theta}}_n) = \mathbf{0} \tag{47}$$

At the next time step t_{n+1}, we require the residual to vanish

$$\mathbf{R}_{n+1} = \mathbf{R}(\mathbf{z}_{n+1}) = \mathbf{0} \tag{48}$$

The resulting nonlinear system is solved using Newton's method to find an approximate solution $\mathbf{z}_{n+1}^{(j+1)}$ in an iterative manner

$$\mathbf{z}_{n+1}^{(j+1)} = \mathbf{z}_{n+1}^{(j)} - [\mathbf{K}(\mathbf{z}_{n+1}^{(j)})]^{-1} \mathbf{R}_{n+1}^{(j)} \tag{49}$$

with the tangent matrix defined as

$$\mathbf{K}(\mathbf{z}_{n+1}^{(j)}) = \left. \frac{\partial \mathbf{R}}{\partial \mathbf{z}_{n+1}} \right|_{\mathbf{z}_{n+1}^{(j)}} \tag{50}$$

Here, superscript j represents the Newton iteration step, while subscript n denotes the time step. By defining the increment $\delta\mathbf{z} = \mathbf{z}_{n+1}^{j+1} - \mathbf{z}_{n+1}^{(j)}$, Eq. (49) can be written as

$$\mathbf{R}_{n+1}^{(j)} - \mathbf{K}(\mathbf{z}_{n+1}^{(j)}) \delta\mathbf{z} = \mathbf{0} \tag{51}$$

The thermo-mechanical-damage coupled system is solved using a staggered iteration algorithm. For each time step from t_n to t_{n+1}, we iterate through the following steps at iteration j:

- Step 1: The mechanical-thermal coupled subproblem
  Keep the damage field $\tilde{\mathbf{d}}_{n+1}^{(j-1)}$ fixed from the previous iteration and based on the discretized governing equations of the thermo-mechanical coupled problem given in Eqs. (42) and (47), the residual vectors for displacement and temperature fields are

$$\mathbf{r}_u(\tilde{\mathbf{u}}_{n+1}^{(j)}) = \mathbf{f}_{u,n+1}^{\mathrm{ext}} - \int_\Omega \mathbf{B}_u^T \boldsymbol{\sigma} \mathrm{d}\Omega = \mathbf{0}, \;\; \boldsymbol{\sigma} = \boldsymbol{\sigma}(\tilde{\mathbf{u}}_{n+1}^{(j)}, \tilde{\boldsymbol{\theta}}_{n+1}^{(j)}, \tilde{\mathbf{d}}_{n+1}^{(j-1)}) \tag{52}$$

$$\mathbf{r}_\theta(\tilde{\boldsymbol{\theta}}_{n+1}^{(j)}) = \Delta t \mathbf{f}_{\theta,n+1}^{\mathrm{ext}} + \Delta t \int_\Omega \mathbf{B}_\theta^T \mathbf{q} \mathrm{d}\Omega - \mathbf{C}(\tilde{\boldsymbol{\theta}}_{n+1} - \tilde{\boldsymbol{\theta}}_n) = \mathbf{0}, \;\; \mathbf{q} = \mathbf{q}(\tilde{\boldsymbol{\theta}}_{n+1}^{(j)}, \tilde{\mathbf{d}}_{n+1}^{(j-1)}) \tag{53}$$

  The linearized system for the coupled problem takes the form

$$\begin{bmatrix} \mathbf{K}^{uu} & \mathbf{K}^{u\theta} \\ \mathbf{0} & \mathbf{K}^{\theta\theta} \end{bmatrix} \begin{bmatrix} \delta\tilde{\mathbf{u}} \\ \delta\tilde{\boldsymbol{\theta}} \end{bmatrix} = \begin{bmatrix} \mathbf{r}_u \\ \mathbf{r}_\theta \end{bmatrix} \tag{54}$$

where the stiffness matrices are defined as

$$\mathbf{K}^{uu} = \int_{\Omega} \mathbf{B}_u^{\mathrm{T}} \left(\frac{\partial \boldsymbol{\sigma}}{\partial \boldsymbol{\varepsilon}} \right) \mathbf{B}_u \mathrm{d}\Omega \tag{55}$$

$$\mathbf{K}^{u\theta} = \int_{\Omega} \mathbf{B}_u^{\mathrm{T}} \left(\frac{\partial \boldsymbol{\sigma}}{\partial \theta} \right) \mathbf{N}_\theta \mathrm{d}\Omega \tag{56}$$

$$\mathbf{K}^{\theta\theta} = \Delta t \int_{\Omega} \mathbf{B}_\theta^{\mathrm{T}} k \mathbf{B}_\theta \mathrm{d}\Omega + \mathbf{C} \tag{57}$$

where $k = \mathbf{g}(d)k_0$ is the degraded thermal conductivity coefficient. It is notable that the temperature induced strain is taken into account in the model, whereas the strain/stress has no influence on heat conduction.

- Step 2: The phase field subproblem (quasi-static)
  Using the updated displacement field $\tilde{\mathbf{u}}^{(j)}_{n+1}$ and temperature field $\tilde{\theta}^{(j)}_{n+1}$, we solve for the nodal damage field $\tilde{\mathbf{d}}^{(j)}_{n+1}$ in the phase field subproblem

$$\mathbf{r}_d(\tilde{\mathbf{d}}^{(j)}_{n+1}) := \int_{\Omega} \mathbf{N}_d^{\mathrm{T}} \mathbf{Q} \mathrm{d}V - \int_{\Theta} \mathbf{B}_d^{\mathrm{T}} \mathbf{g} \mathrm{d}\Theta, \;\; \mathbf{Q} = \mathbf{Q}(\tilde{\mathbf{u}}^{(j)}_{n+1}, \tilde{\theta}^{(j)}_{n+1}, \tilde{\mathbf{d}}^{(j)}_{n+1}), \;\; \mathbf{g} = \mathbf{g}(\tilde{\mathbf{d}}^{(j)}_{n+1}) \tag{58}$$

The linearized equation can be written as

$$\mathbf{K}^{dd} \delta \tilde{\mathbf{d}} = \mathbf{r}_d \tag{59}$$

with

$$\mathbf{K}^{dd} = \int_{\Theta} \left[\mathbf{N}_d^{\mathrm{T}} \left(-\frac{\partial \mathbf{Q}}{\partial d} \right) \mathbf{N}_d + \frac{2l_0}{c_0} \mathbf{B}_d^{\mathrm{T}} \mathbf{B}_d \right] \mathrm{d}\Theta \tag{60}$$

While the governing equations for temperature and crack propagation are both time-dependent, with crack propagation typically occurring at a much faster rate than thermal diffusion, our staggered solution algorithm employs a carefully controlled time-stepping approach . To ensure solution accuracy and numerical stability, we implement a damage-based convergence criterion [41]:

$$\left| \tilde{u}^{(j+1)}_{n+1} - \tilde{u}^{(j)}_{n+1} \right| < \varepsilon, \quad \varepsilon = 1.0 \times 10^{-5} \tag{61}$$

This criterion requires that the L^2-norm difference between consecutive iterations falls below a strict tolerance threshold before proceeding. Although this approach necessitates very small load steps and results in slower convergence rates, it provides superior numerical robustness for solving the coupled phase-field and thermal-mechanical problems.

This thermo-mechanically coupled phase-field fracture model is implemented through Abaqus subroutines written in FORTRAN. The solution process starts with using the built-in Abaqus solver to solve the temperature–displacement coupled problem, followed by extracting material point data including displacements, temperatures, and corresponding energies, while updating state variables and field values to control damage effects on material properties. Subsequently, based on the previously calculated history energy, the phase-field values at material points are computed and fed back into the solution. This alternating iteration process drives the degradation of material properties and the evolution of the phase field. Through this methodology, we can output the stress–strain response of solids considering thermo-mechanical damage and phase-field values, thus revealing mechanical and fracture behavior of structures under mixed-mode failure.

3. Preparation and processing of porous sintered silver structure

The pore morphology in sintered silver materials is significantly influenced by various sintering process parameters during manufacturing, including sintering temperature, time, and pressure. The porous microstructure model for numerical analysis in this study is constructed based on SEM micrographs of sintered silver solder (see Fig. 3). Fig. 3(a) presents the SEM micrograph of sintered silver structure with a porosity of 8%. The processing procedure consists of several steps: first, the SEM image given in Fig. 3(a) is binarized using MATLAB to obtain the structure shown in Fig. 3(b). The binarized porous structure is then processed to extract the structural contours of sintered silver. These contours are imported into CAD software for geometric modeling, resulting in the final porous structure shown in Fig. 3(c). This geometric model is then imported into Abaqus for subsequent numerical simulations.

4. Numerical results and discussion

In the following numerical examples, we adopt a sequential validation approach. Examples 4.1–4.3 focus exclusively on mechanical loading responses without temperature effects, allowing us to thoroughly validate the mechanical aspects of our model. Temperature effects are then incorporated in Example 4.4, where we present a comprehensive analysis of coupled thermal-mechanical behavior in sintered silver structures. This progressive approach enables systematic verification of our numerical framework, from pure mechanical response to fully coupled thermal-mechanical interactions.

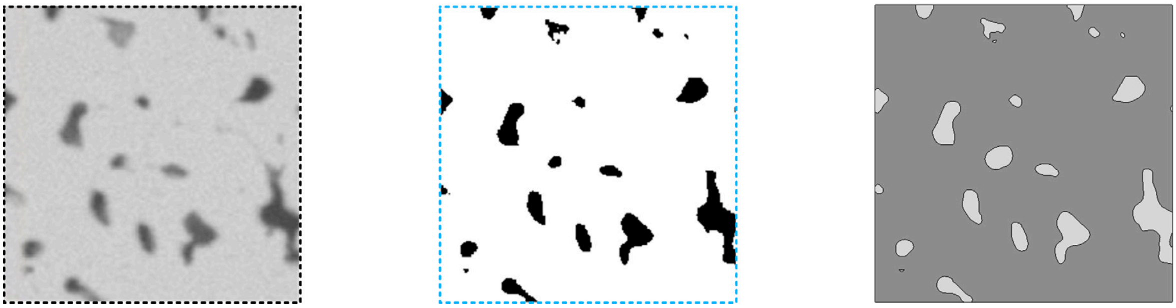

(a) (b) (c)

Fig. 3. Processing steps of porous sintered silver structure: (a) Original SEM image, (b) Binary image after MATLAB processing, (c) Final geometric model for simulation.

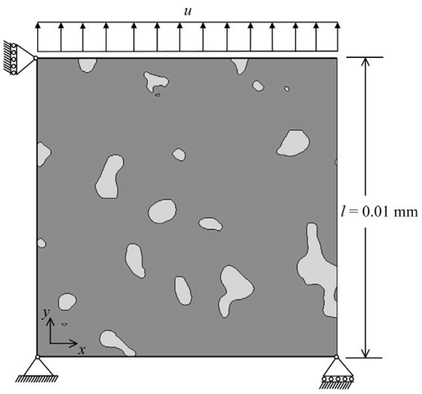

Fig. 4. Boundary conditions of the sintered silver model with 8% porosity: prescribed displacement loading and fixed constraints.

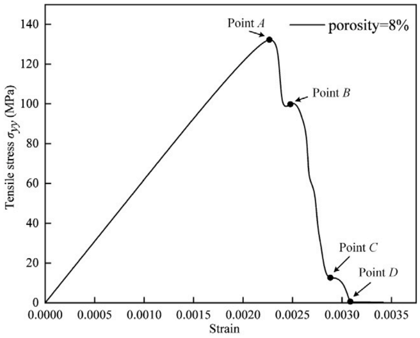

Fig. 5. Stress–strain curve of sintered silver with 8% porosity showing four critical time points.

4.1. Tensile failure analysis

Using the phase-field approach, we investigate the mechanical response and fracture evolution characteristics of sintered silver with 8% porosity. The computational model featuring stochastic pore distribution is reconstructed from selected SEM micrographs. The porous structural model is then implemented in Abaqus finite element software for numerical analysis. Fig. 4 illustrates the applied boundary conditions for the model. The model uses a mesh size of $h = 4\times10^{-5}$ mm, displacement increment $\Delta u = 7\times10^{-7}$ mm, length scale parameter $l_0 = 0.0002$ mm, total time of 1.00, and time increment step of 0.0005. Meanwhile, material parameters for the random porous structure are set in the inp file, as shown in Table 1, which includes both solid sintered silver phase and void phase, along with parameters such as fracture energy G_c, tensile strength f_t, and critical shear-tension ratio χ [19]. Following the methodology established in paper [22], we define void phase as an actual air phase in the material system, representing the physical cavities rather than a mathematical abstraction in the numerical model.

Table 1
Material properties of sintered silver microstructure model.

Parameters	Solid phase	Void phase
Young's modulus (E, GPa)	81.5	8.15×10^{-7}
Poisson's ratio (ν)	0.38	0.38
Fracture surface energy (G_c, MPa × mm)	0.0024	2.4×10^{-11}
Tensile strength (f_t, MPa)	300	3×10^{-6}
Critical shear ratio (χ)	0.60	0.60

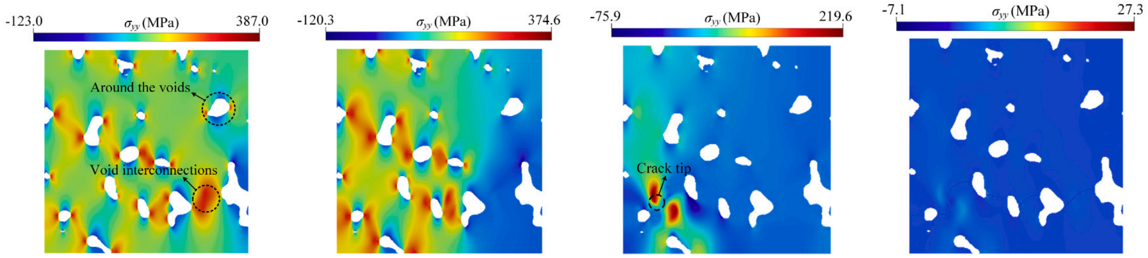

(a) Time point A (b) Time point B (c) Time point C (d) Time point D

Fig. 6. Stress distributions at four critical time points (A - D) marked in Fig. 5.

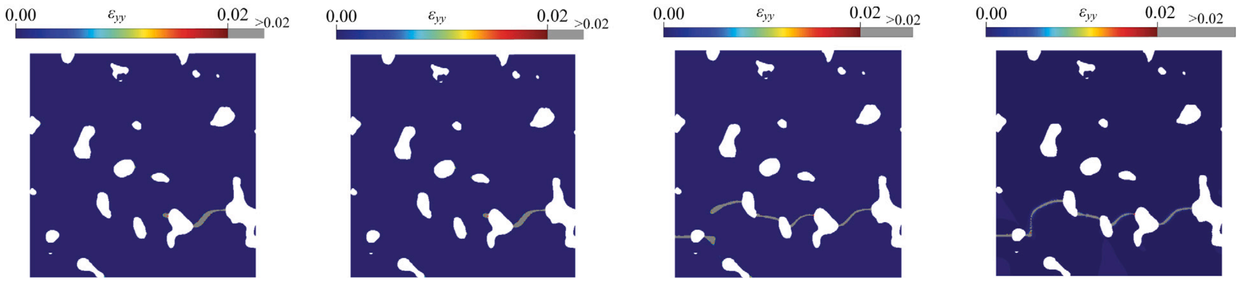

(a) Time point A (b) Time point B (c) Time point C (d) Time point D

Fig. 7. Evolution of strain distribution in porous sintered silver at four loading stages: (a) elastic deformation, (b) onset of localization, (c) strain concentration, and (d) final failure.

Fig. 5 shows the stress–strain curve of the specimen with 8% porosity obtained by current numerical scheme. Four critical time points (A, B, C, and D) are selected on the curve, and their corresponding stress, strain, and phase-field distributions are shown in Figs. 6–8, respectively. The contour results reveal that stress concentrations primarily occur in three regions: around the voids, at void interconnections, and at crack tips. The high strain fields are predominantly localized in the vicinity of cracks. Correspondingly, elevated phase-field values are observed in these regions of stress and strain concentrations, indicating the correlation between mechanical field concentrations and damage evolution. The specimen reaches its maximum tensile strength of 132.0 MPa at a strain of 0.23% (at point A in Fig. 5), where the phase-field value d attains a value of 1.0, signifying the onset of crack formation. The corresponding phase-field distribution is illustrated in Fig. 8(a). As the loading progresses from point A to point B, the first crack initiates in the structure, with its location illustrated in Fig. 8(b). This crack formation is accompanied by a stress reduction to 98.8 MPa. The progression from point B to point C is characterized by continuous crack propagation through the sintered silver structure, resulting in a dramatic decrease in stress to 12.68 MPa. From point C to point D, the crack continues to propagate with stress decreasing to 0 MPa, as the crack completely penetrates the entire structure. Five cracks are ultimately formed as shown in Fig. 8(d). At this point, with a failure strain of 0.31%, the sintered silver structure experiences complete failure. The analysis reveals that the maximum tensile strength of sintered silver is critically linked to the formation of the first crack, which initiates at the structure's most vulnerable region. Following crack initiation, the structure experiences a significant reduction in overall stress, accompanied by rapid crack propagation. This progressive deterioration process eventually culminates in complete structural failure.

For further validation of the proposed phase-field approach, multiple random specimens are analyzed. Six groups of sintered silver models with porosity variations from 8% to 30% are subjected to phase-field fracture simulation. The corresponding stress–strain relationships, demonstrating the effect of porosity on mechanical behavior, are illustrated in Fig. 9. As illustrated in Fig. 9, the stress–strain behavior of sintered silver structures with varying porosity levels exhibits significant differences primarily in two aspects: (1) The elastic stage characteristics from initial loading to crack initiation; (2) The maximum tensile strength values attained before failure. These variations directly reflect the influence of porosity on the mechanical properties of sintered silver structures. When the strain is below 0.2%, all sintered silver structures, regardless of their porosity levels, remain damage-free

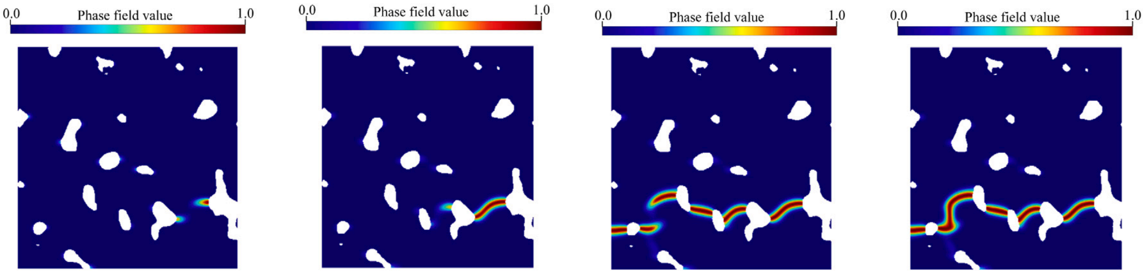

(a) Time point A (b) Time point B (c) Time point C (d) Time point D

Fig. 8. Contour plots of phase-field damage parameter d showing the progression of damage in porous sintered silver at four critical time points. The damage parameter ranges from $d = 0$ (intact material, blue) to $d = 1$ (completely damaged, red).

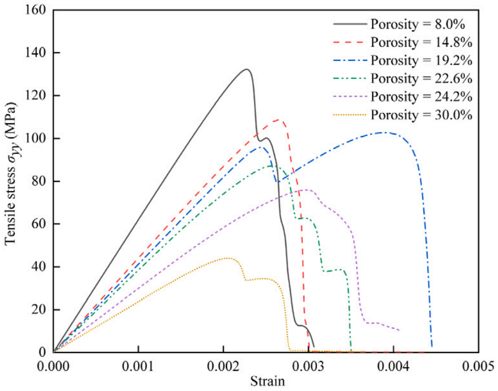

Fig. 9. Stress–strain curves of sintered silver structures with different porosity levels. The decreasing trend in strength and stiffness corresponds to increasing porosity.

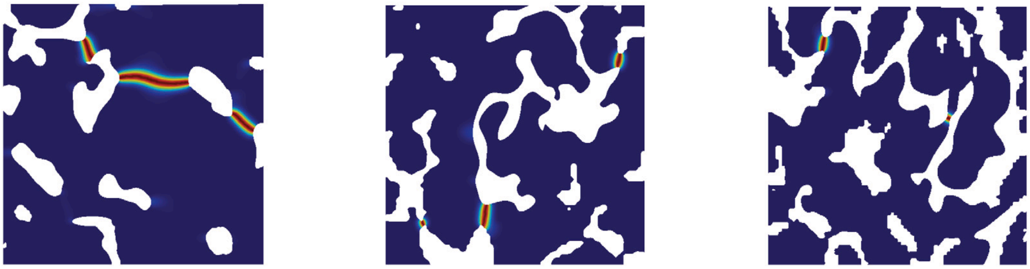

(a) 14.8% porosity (b) 24.2% porosity (c) 30% porosity

Fig. 10. Simulated crack morphologies in sintered silver structures with varying porosity levels.

with no damaged elements present. In this elastic regime, the structural stiffness demonstrates a direct correlation with porosity: as the porosity increases, the elastic modulus exhibits a steady decline from 61,990 MPa to 10,624 MPa, indicating a clear porosity-dependent mechanical behavior. The maximum tensile strength demonstrates a clear dependence on porosity levels: as porosity increases from 8% to 30%, a significant reduction in maximum tensile strength is observed, declining from 132.2 MPa to 32.80 MPa, following a consistent downward trend.

The simulated crack patterns presented in Fig. 10 reveal a distinct correlation between porosity and crack morphology: (1) At lower porosity levels: formation of larger, more continuous cracks; (2) At higher porosity levels: development of multiple smaller cracks predominantly between void regions; (3) The transition in crack patterns reflects the influence of porosity on damage evolution mechanisms.

To ensure results' reliability, in Fig. 11, a comparative analysis was conducted between the current numerical predictions and existing experimental data from literature [10,13,14,19,47,48]. The mechanical properties, including elastic modulus and tensile strength, were evaluated across various porosity levels. The comparison reveals consistent trends in both numerical and experimental results regarding the relationship between mechanical properties and porosity. However, the numerically predicted elastic modulus

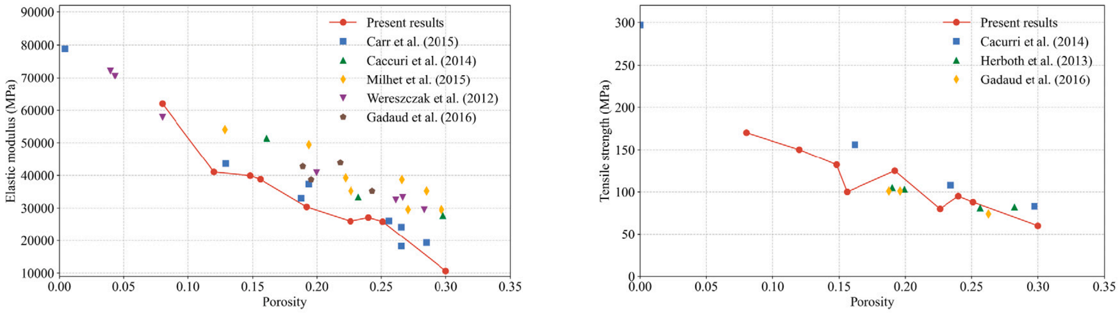

(a) Elastic modulus (b) Tensile strength

Fig. 11. Comparative analysis of elastic modulus: present numerical results versus experimental data from literature [10,13,14,19,47,48].

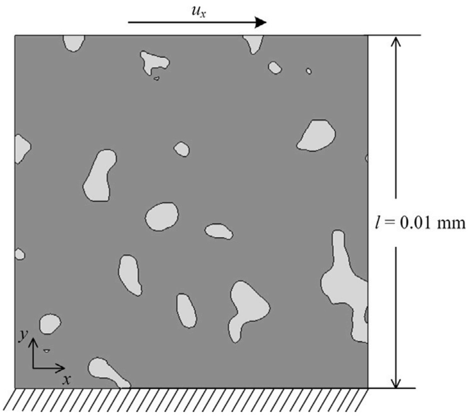

Fig. 12. Boundary conditions for shear loading simulation of sintered silver structure.

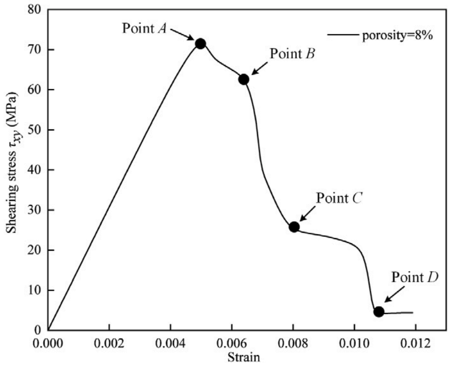

Fig. 13. Stress–strain curve under shear loading for sintered silver structure with 8% porosity.

values are slightly lower than some experimental measurements. This discrepancy can be attributed to the relatively conservative baseline silver properties adopted in Table 1.

4.2. Shear failure analysis

The phase-field model is further employed to investigate the mechanical response and fracture evolution of 8% porosity sintered silver under shear loading conditions. The boundary conditions is illustrated in Fig. 12. Similar to the above tensile failure simulation, the bottom edge is fixed, and a displacement load parallel to the x-direction is applied to the upper boundary. Other simulation parameters remain identical to those used in the tensile failure analysis of Section 4.1.

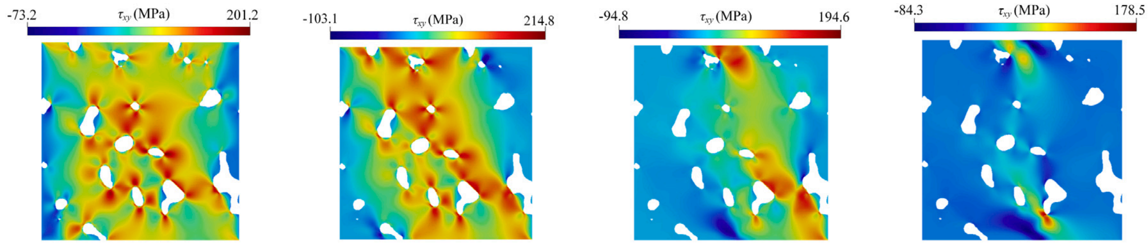

(a) Point A (b) Point B (c) Point C (d) Point D

Fig. 14. Stress distributions at four critical time points under shear loading.

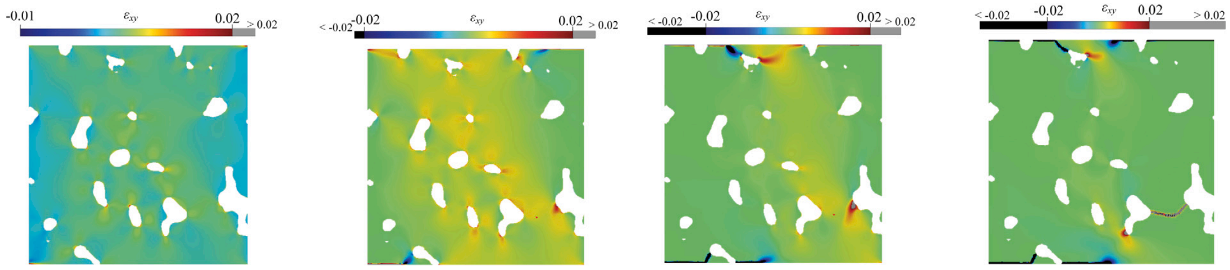

(a) Point A (b) Point B (c) Point C (d) Point D

Fig. 15. Evolution of strain fields at four critical loading stages.

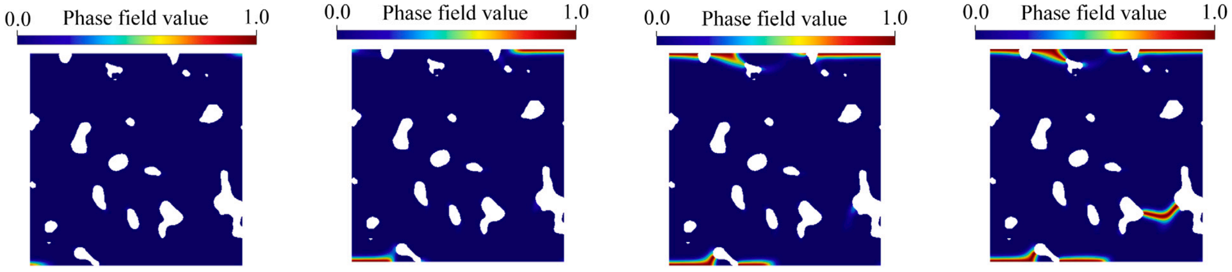

(a) Point A (b) Point B (c) Point C (d) Point D

Fig. 16. Evolution of phase-field damage parameter under shear loading.

Fig. 13 shows the stress–strain curve of the specimen with 8% porosity under shear loading. Four critical time points are selected on the curve, and their corresponding stress, strain, and phase-field distributions are shown in Figs. 14, 15, and 16, respectively. Analysis of the contour plots reveals distinct patterns of stress and strain localization. High shear stresses are also predominantly concentrated in three critical regions: around the voids, at void interconnections, and at crack tips. Correspondingly, significant strain concentrations are observed in the vicinity of crack regions. These localized mechanical fields indicate potential paths for damage evolution and crack propagation. A critical state is observed when the shear strain reaches 0.5%, at which point three significant phenomena occur simultaneously: (1) The structure attains its maximum shear strength of 71.3 MPa; (2) The phase-field damage parameter reaches its critical value of 1.0; (3) Crack propagation initiates. The phase-field distribution corresponding to this critical state is presented in Fig. 16(a). As the loading progresses from point A to B, the structure exhibits distinct damage evolution characteristics under shear loading. Two cracks develop simultaneously at the upper and lower surfaces of the specimen, accompanied by a reduction in stress to 65.2 MPa. During the progression from point B to C, crack propagation continues along the sintered silver structure, resulting in a dramatic decrease in stress from 65.2 MPa to 24.8 MPa, indicating significant structural degradation. The transition from point C to D represents the final failure stage, characterized by continued crack propagation leading to almost complete structural failure of the sintered silver. The stress level drops to 4.2 MPa, and the resulting crack pattern is presented in Fig. 16(d).

The comparison of stress–strain responses under different loading conditions, as shown in Fig. 17, reveals distinctive mechanical behavior and failure characteristics. The tensile loading exhibits higher maximum strength but lower failure strain compared to shear loading. Additionally, the failure mechanisms differ significantly between the two loading conditions: tensile loading leads to rapid crack propagation and sudden failure, while shear loading results in gradual crack growth and progressive failure development.

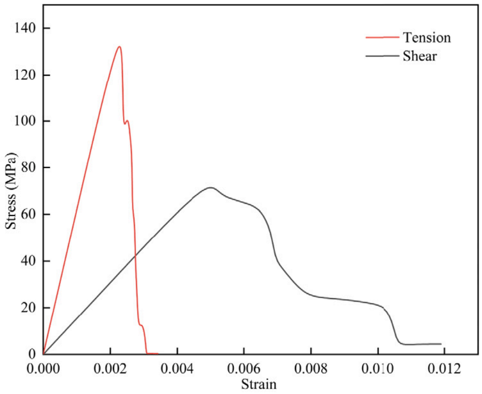

Fig. 17. Stress–strain responses of sintered silver structure with 8% porosity under tensile and shear loading.

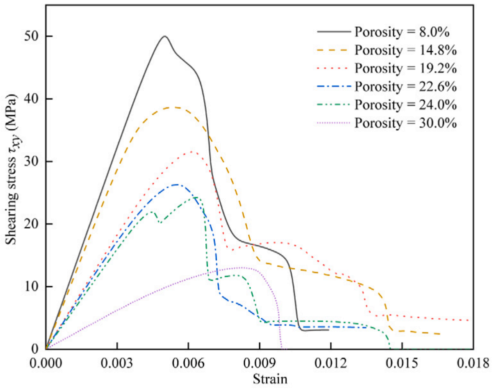

Fig. 18. Stress–strain responses of sintered silver structures with different porosity levels under shear loading.

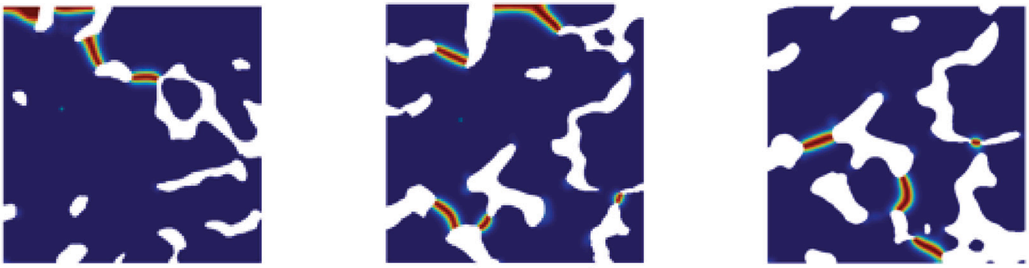

(a) 12% porosity (b) 16% porosity (c) 24% porosity

Fig. 19. Crack propagation paths in sintered silver structures with different porosity levels under shear loading.

Shear failure analysis was conducted on six groups of sintered silver structures with different porosity levels. The stress–strain responses are shown in Fig. 18. The shear modulus and maximum shear strength follow the same trend as observed under tensile loading, both decreasing with increasing porosity. Fig. 19 shows the crack propagation paths for sintered silver structures with different porosity levels under shear loading. At lower porosity, failure primarily occurs along the boundaries, while with increasing porosity, cracks tend to develop at weak regions between voids.

4.3. Validation against end-notched flexure (ENF) test results

The ENF test, originally developed by Russell [49], employs a three-point bending configuration on double cantilever beam specimens for Mode II fracture toughness evaluation. This testing methodology has gained widespread acceptance for characterizing Mode II interlaminar fracture toughness, particularly in composite laminates and adhesive materials. The effectiveness of ENF

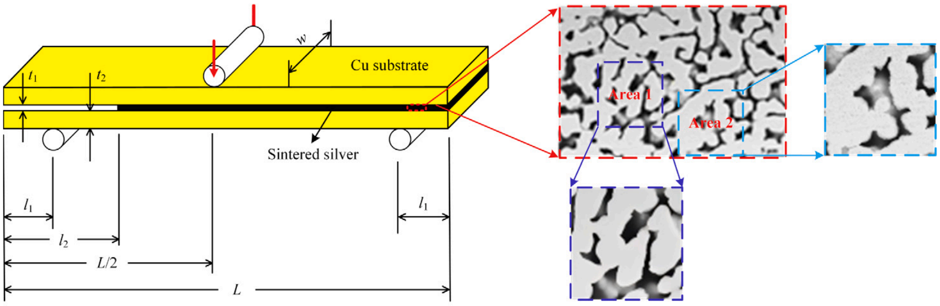

Fig. 20. ENF test specimen geometry with parameter definitions (left) and SEM micrograph of sintered silver showing two selected regions (10 μm × 10 μm) with 24.5% and 24.8% porosity (right).

Table 2
Parameters and dimensions of ENF test specimen.

Parameter	Description	Dimension (mm)
L	Total length	100.0
l_1	Distance from support to end	10.0
l_2	Initial crack length	30.0
t_1	Thickness of sintered silver layer	0.1
t_2	Thickness of copper substrate	1.2
w	Specimen width	8.0

testing in characterizing shear fracture behavior has been well established. Building on this foundation, Zhao et al. [18] conducted comprehensive ENF experiments specifically focused on sintered silver solder. Our numerical simulations are designed to replicate and analyze their experimental conditions. The ENF test configuration comprises a layered structure of copper substrates and sintered silver solder. The geometric configuration and dimensional parameters of the test specimen are illustrated in the left of Fig. 20, with the corresponding parameter definitions and magnitudes detailed in Table 2. The specimen consists of upper copper substrate, sintered silver solder layer and lower copper substrate.

In this example, we adopt a two-scale simulation approach instead of direct phase-field modeling at the macroscopic level. The simulation procedure consists of two sequential steps: (1) microscale phase-field simulations are performed to obtain the mechanical properties of sintered silver, and (2) these properties are then incorporated into the macroscopic ENF structure through numerical homogenization for static analysis. The apparent plastic response observed in the force–displacement curve is attributed to the contact interaction between the indenter and the Cu substrate, rather than a change in the material constitutive model. This behavior is consistent with previous experimental observations reported in [18].

In this example, two regions of 10 μm × 10 μm (Area 1 and 2) are selected from the SEM image shown in the right of Fig. 20, with porosity levels of 24.5% and 24.8% respectively. These images were taken under sintering conditions of 300 °C temperature and 60 min duration, which typically results in a porosity of 24.08% ±0.84% in the sintered silver layer [18]. The selected SEM images were obtained under these sintering conditions and satisfy the corresponding porosity requirements. Then the mechanical properties of the sintered silver structure were determined through phase-field simulations based on the loading conditions shown in Fig. 21. Two sets of elastic moduli were calculated in both x and y directions (E_{xx} and E_{yy}). The average of these four values yielded an elastic modulus of 15,105 MPa. The corresponding Poisson's ratio was experimentally determined to be 0.22, as reported in the literature [47].

The finite element model and boundary conditions for the ENF test simulation are illustrated in Fig. 22. The mechanical properties of the materials are specified as follows: the supports and loading head are defined as rigid bodies, while the copper substrate is characterized by an elastic modulus of 115 GPa, Poisson's ratio of 0.236, yield strength of 219 MPa, and tangent modulus of 6.5 GPa. The simulation incorporates the previously determined parameters ($E = 15.105$ GPa, $\mu = 0.22$) for the sintered silver layer. Fig. 23 shows the force–displacement curves obtained from both simulation and experiments. The simulation results fall well within the experimental data range, demonstrating the feasibility of using microscale simulation data of sintered silver to evaluate macroscopic mechanical properties of the structure.

4.4. Thermal loading induced failure of sintered silver structure

As shown in Fig. 24, a typical power module structure consists of silicon chip, sintered silver layer, and DBC structure from top to bottom. The material parameters of chip, sintered silver, copper, and ceramic are listed in Table 3, while the phase-field fracture parameters of sintered silver remain the same as in Table 1. This case study will utilize the thermo-mechanical coupled phase-field fracture model to analyze the fracture evolution process of sintered silver during power device service.

As illustrated in Fig. 25, the structural model features a sintered silver layer with 12.5% porosity. For the mechanical constraints, symmetric boundary conditions are applied in the horizontal direction on both left and right boundaries, while the bottom surface is

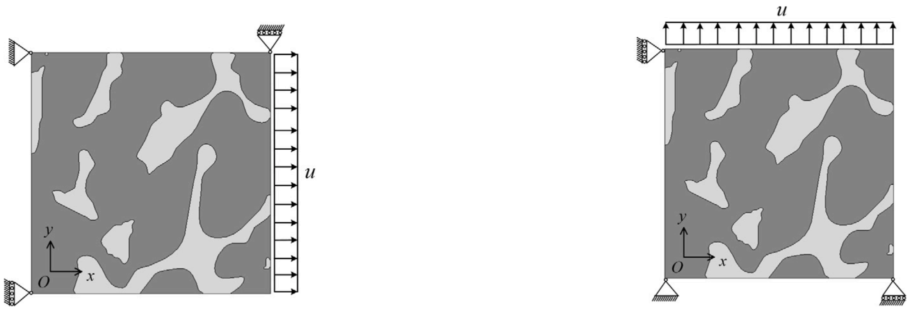

(a) Loading along x-direction

(b) Loading along y-direction

Fig. 21. Schematic diagram of boundary conditions and loading configurations for sintered silver model in x and y directions.

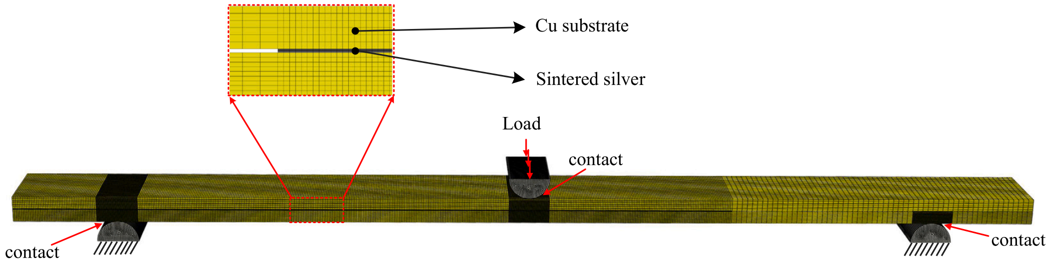

Fig. 22. Finite element model and boundary conditions for ENF test simulation.

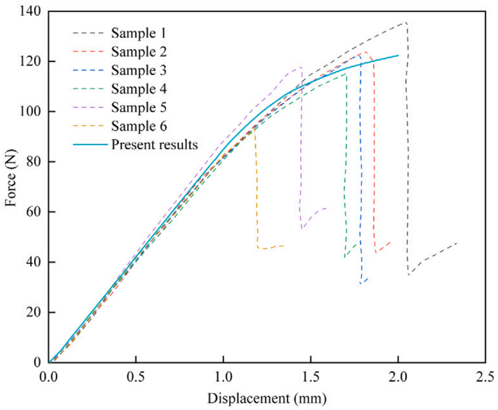

Fig. 23. Comparison of force–displacement curves between numerical simulation and experimental results.

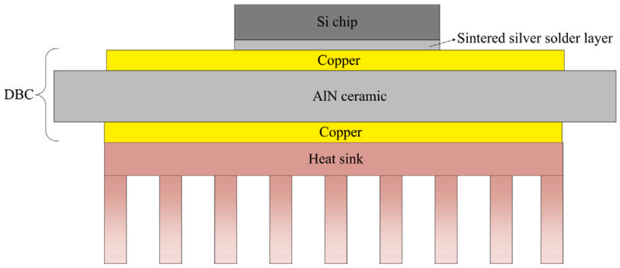

Fig. 24. Schematic diagram of typical power module structure.

Table 3
Material properties of power module components.

Material	E (GPa)	ν –	ρ (kg/m^3)	k (W/m K)	c_p (J/kg K)	α_0 (ppm/°C)
Si	162.0	0.28	2330	130.00	700	3.00
Sintered Ag	81.5	0.38	1040	418.00	170	18.90
Cu	110.0	0.35	8960	400.00	385	17.00
AlN ceramic	348.0	0.27	3340	177.00	820	5.60

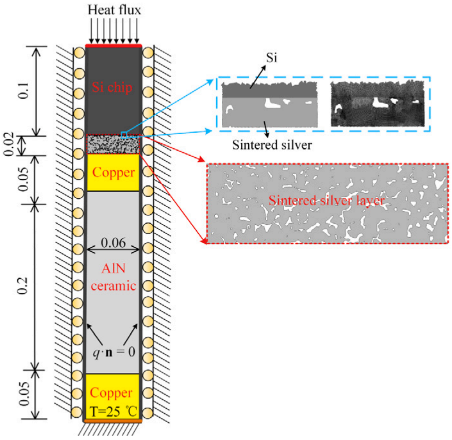

Fig. 25. Finite element model and prescribed thermal-mechanical boundary conditions for power module simulation (all dimensions are given in mm).

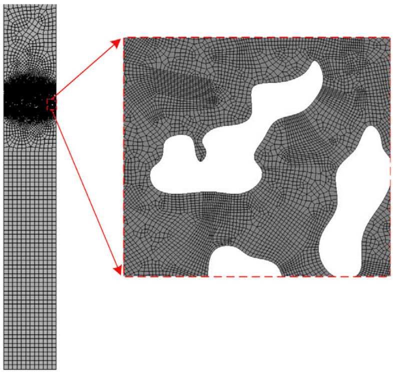

Fig. 26. Mesh discretization of power module structure: global view with zoomed-in detail showing refined mesh in sintered silver layer region.

fixed. The thermal loading conditions are implemented through a surface heat source on the chip with a heating rate of 60 °C/min, adiabatic conditions on the lateral surfaces, and a constant temperature of 25 °C maintained at the bottom surface to simulate the heat sink effect. The finite element discretization of the power module structure for phase-field fracture analysis is illustrated in Fig. 26. A refined mesh with size $h = 6 \times 10^{-5}$ mm is applied to the sintered silver layer, where the characteristic length l_0 is set as 0.0003 mm. A coarser mesh size of 0.005 mm is used for other structural components. The complete model comprises 454,104 coupled temperature–displacement quadrilateral elements and an equal number of four-node User UEL elements, where the phase-field values are determined based on the displacement and temperature fields. Perfect bonding conditions are imposed at all material interfaces. The simulation is conducted over a period of 500 s using a time increment of 1 s.

The field distributions in the sintered silver layer at chip surface temperature of 125 °C are presented in Fig. 27. The temperature distribution (Fig. 27(a)) exhibits a gradual decrease from the silicon chip surface downward, with local fluctuations due to the underlying microstructural heterogeneity. The stress distributions, shown in Figs. 27(b), 27(c), and 27(d), reveal significant stress concentrations in the vicinity of voids and their interconnecting regions. These localized high stresses, through the energy functional mechanism, induce elevated phase-field values at material points within the sintered silver structure. The progressive increase in phase-field values driven by these stress concentrations ultimately leads to material failure, indicating potential crack initiation sites. This prediction is corroborated by subsequent simulations showing crack initiation preferentially occurring at locations of elevated phase-field values within the microporous structure.

(a) Temperature field

(b) Normal stress σ_{xx}

(c) Normal stress σ_{yy}

(d) Shear stress τ_{xy}

Fig. 27. Temperature and stress field distributions in sintered silver layer under thermal loading.

(a) Surface temperature: 125℃

(b) Surface temperature: 225℃

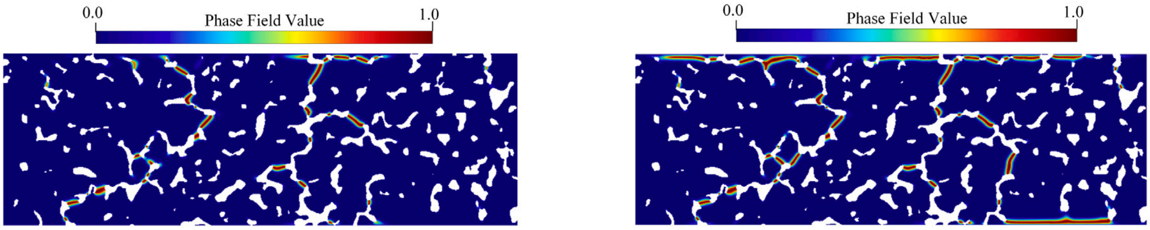

(c) Surface temperature: 325℃

(d) Surface temperature: 500℃

Fig. 28. Evolution of phase-field values in sintered silver at different temperatures showing progressive damage development.

Fig. 28 shows the phase-field distributions in the sintered silver layer at chip surface temperatures of 125 °C, 225 °C, 325 °C, and 500 °C. Note that temperatures higher than typical operational ranges are used to demonstrate failure mechanisms, as the present model does not incorporate fatigue effects. As shown in Fig. 28(a), elevated phase-field values appear in high-stress regions near void throats. When the chip surface temperature reaches 155 °C, the phase-field value in the solder layer reaches 1.0, indicating crack initiation. As the chip surface temperature further increases to 225 °C, cracks continue to propagate perpendicular to the chip direction, as shown in Fig. 28(b). This propagation direction results from horizontal thermal stresses generated during chip heating, due to the difference in thermal expansion coefficients (CTE) between the sintered silver layer and first copper layer (CTE of sintered silver: 18.90, copper: 17.00) compared to the silicon chip (CTE: 3.00). These horizontal thermal stresses provide the driving force for crack propagation toward the chip direction. As shown in Fig. 28(c), when the chip surface temperature rises to 325 °C, distinct cracks have formed at weak connections in the sintered silver solder layer. With further temperature increase, cracks begin to propagate horizontally along interfaces, extending along both the bottom surface of the silicon chip and the top surface of the first copper layer, as illustrated in Fig. 28(d).

In our work, we model thermal conductivity degradation in damaged regions through Eq. (37), which effectively prevents heat flow across crack surfaces. As illustrated in Fig. 29, the evolution of heat flow in the sintered silver structure demonstrates this

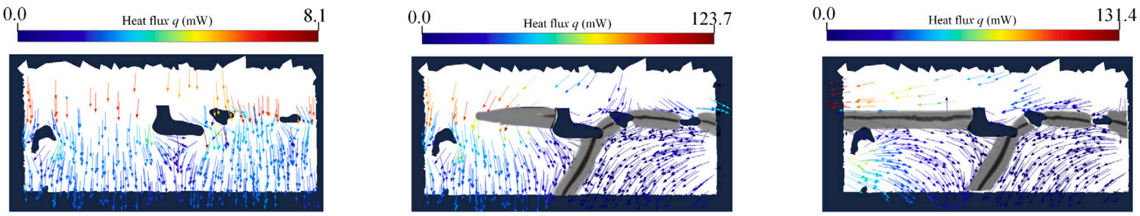

(a) Undamaged state (b) Initial crack formation (c) Final temperature distribution

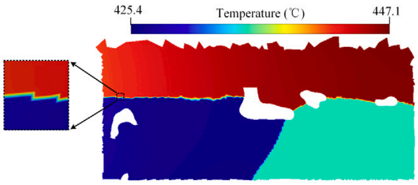

(d) Final heat flow distribution

Fig. 29. Heat flow patterns in sintered silver structure demonstrating the evolution of thermal conductivity degradation (The location of the model is shown in the blue dashed square of Fig. 26).

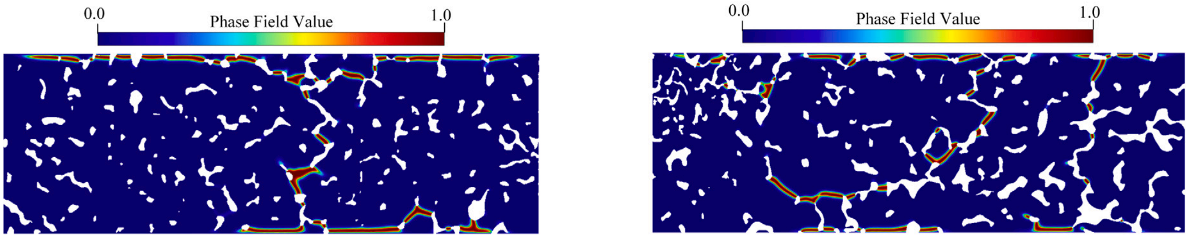

(a) Porosity = 9.1% (b) Porosity = 13.1%

Fig. 30. Comparison of phase-field values distributions in sintered silver with different porosity levels under thermal loading.

thermal barrier effect. Fig. 29(a) shows the initial uniform heat flux distribution in the undamaged state. During crack formation, as shown in Fig. 29(b), the heat flux pattern changes significantly, with heat flow beginning to divert around the developing crack. Fig. 29(c) reveals the final heat flux distribution with a distinct discontinuity across the fully developed crack. The temperature field shown in Fig. 29(d) further confirms this behavior - heat flow is forced to circumvent the crack surface rather than passing through it, demonstrating the effectiveness of our thermal conductivity degradation model in capturing the thermal barrier effect of cracks.

For further validation of the simulation results, additional analyses were conducted using two random sintered silver structures with porosities of 9.1% and 13.1%. The PF values, illustrated in Figs. 30(a) and 30(b), reveal consistent crack evolution patterns. The crack initiation and propagation in the sintered silver layer follows a specific sequence driven by both tensile and shear mechanisms. Initially, tensile stresses within the solder layer induce vertical cracks perpendicular to the chip layer. Subsequently, due to the significant thermal expansion coefficient mismatch between sintered silver (18.90 ppm/°C) and silicon chip (3.00 ppm/°C), shear stresses develop and drive crack propagation horizontally along the upper boundary. Finally, crack propagation occurs at the lower boundary, driven by shear stresses arising from the thermal expansion coefficient difference between sintered silver and Cu substrate (17.00 ppm/°C). This sequential development explains the observed horizontal crack patterns at both interfaces, with failure initiating at the upper boundary due to the larger CTE mismatch. Notably, the crack length exhibits asymmetric development, with longer cracks observed near the chip interface compared to those near the copper layer interface.

4.5. Shear failure of chip

Chip shear testing is commonly used to measure the shear strength of sintered silver joints. This section presents phase-field simulations of chip shear tests at different temperatures. Fig. 31(a) shows a schematic diagram of the typical setup for measuring shear strength of sintered silver joints. For computational efficiency, numerical analysis is performed on a representative section, indicated by the green dashed domain in Fig. 31(a). The detailed simulation model with boundary conditions is illustrated in Fig. 31(b), maintaining the same dimensions as the previous section. A horizontal rightward displacement load is applied to the left surface of the chip to simulate the shear probe effect, while symmetric constraints are applied to both left and right surfaces of the DBC structure, and fixed constraints are applied to the bottom surface. Various temperature fields are applied globally to

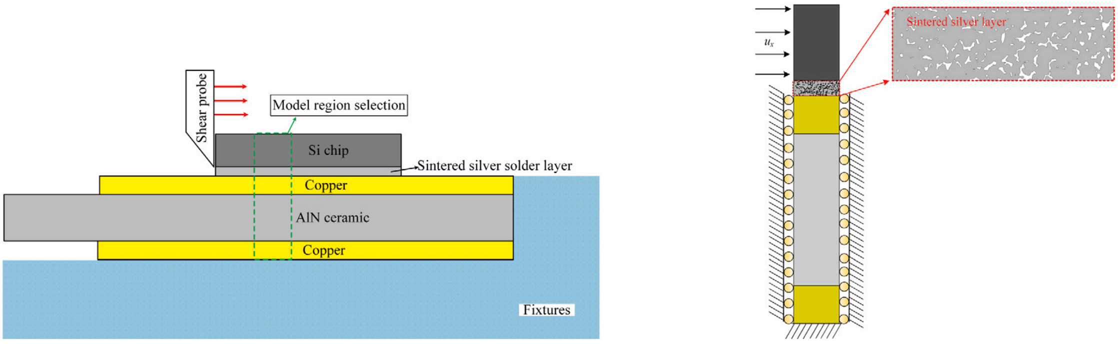

(a) Test setup configuration

(b) Selected region for simulation

Fig. 31. Chip shear test: (a) schematic diagram of experimental setup for measuring shear strength and (b) representative region selected for numerical simulation.

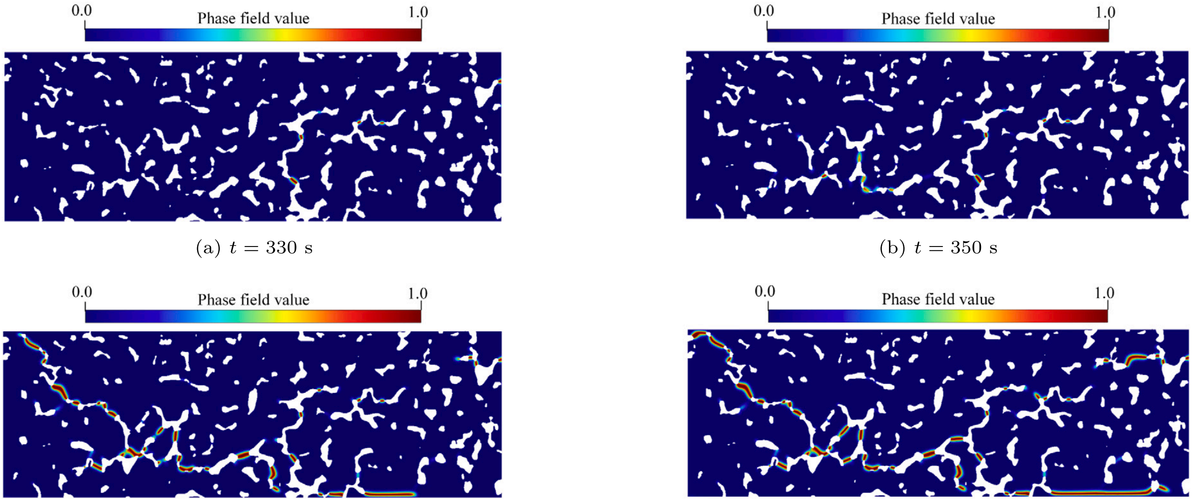

(a) $t = 330$ s

(b) $t = 350$ s

(c) $t = 410$ s

(d) $t = 500$ s

Fig. 32. Crack propagation paths in solder layer during shear testing at room temperature at different time points.

simulate chip shear failure under different temperature conditions. The material parameters and additional simulation details remain consistent with those specified in the previous section.

The crack evolution process in the sintered silver structure under room temperature and shear loading exhibits distinct stages: initial crack nucleation at void interconnections (Fig. 32(a)), formation of multiple microcracks under increasing shear force (Fig. 32(b)), development of major cracks propagating predominantly toward the chip loading end (Fig. 32(c)), and finally, complete structural failure with the characteristic crack pattern shown in Fig. 32(d), indicating total loss of mechanical integrity.

Different shear failure simulations were conducted at temperatures of 25 °C, 75 °C, 150 °C, 225 °C, and 300 °C, with the resulting crack morphologies shown in Fig. 33. As the loading temperature increases, the crack pattern gradually transitions from a wavy pattern to horizontal cracks near the interface. Fig. 34 shows the shear strength at different temperatures, indicating that the chip's shear strength gradually decreases with increasing temperature, reaching only 28% of its room temperature value at 300 °C. This is because when the global temperature of the sintered silver structure rises to 169 °C, the phase-field value reaches 1.0, and cracks continue to propagate under thermal stress with further temperature increase. At 25 °C, 75 °C, and 150 °C, when no cracks have yet formed in the structure, the crack morphology exhibits a wavy pattern. At 225 °C and 300 °C, significant cracks have developed in the sintered silver solder layer under thermal stress, primarily near the silicon chip interface, leading to a substantial decrease in shear strength. Under shear force, these cracks continue to propagate until complete structural failure. It is also observed that crack density is higher near the chip interface compared to the first copper layer interface.

5. Conclusions

This work establishes a thermo-mechanical coupled phase-field fracture model for analyzing random porous structures of sintered silver based on SEM images, which is capable of handling complex mixed-mode fracture involving both tensile and shear failure

(a) $T = 75$°C   (b) $T = 150$°C

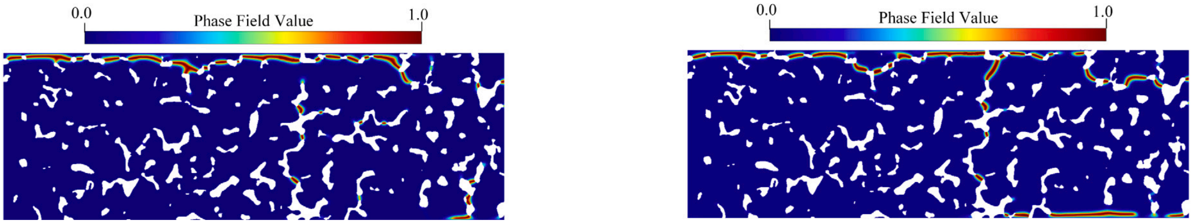

(c) $T = 225$°C   (d) $T = 300$°C

Fig. 33. Crack morphologies in sintered silver layer during shear testing at different temperatures.

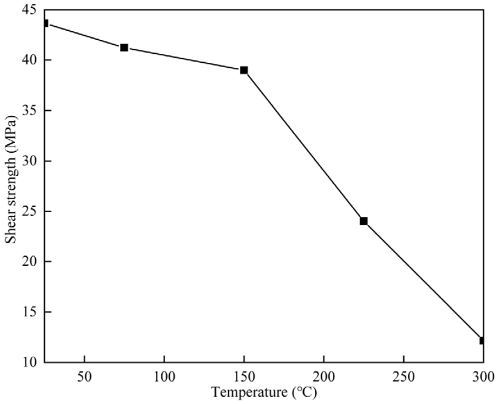

Fig. 34. Temperature dependence of shear strength in sintered silver joints.

under thermo-mechanical coupling. The phase-field simulations demonstrate that both elastic modulus and tensile strength decrease with increasing porosity under both tensile and shear loading conditions. The model predictions show excellent agreement with experimental results through ENF test validation, where microscale analysis of void structures correlates well with macroscopic mechanical responses.

Numerical results also reveal that complex crack networks develop in the sintered silver solder layer under thermal and mechanical loading conditions in power devices. Under thermal loading, cracks initially propagate perpendicular to the chip layer, followed by horizontal interface propagation, exhibiting asymmetric length distribution with longer cracks near the chip surface. During chip shear testing, cracks initiate at weak connections between voids, and their morphology transitions from wavy patterns to horizontal interfacial cracks with increasing temperature, demonstrating distinct temperature-dependent evolution characteristics.

The proposed image-based modeling approach combined with phase-field fracture analysis provides significant insights into the mechanical properties of randomly porous sintered silver materials and the complex mechanisms of crack initiation, propagation, and network formation in solder layers. This methodology offers valuable guidance for understanding and improving the reliability of sintered silver interconnections in electronic packaging applications.

Future work will focus on two major aspects to advance our understanding of thermal-mechanical behavior in sintered silver materials. First, to improve thermal-mechanical coupling analysis, we will investigate: (1) detailed characterization of temperature field evolution near crack surfaces, (2) development of comprehensive heat transfer theories for various crack configurations, and (3) integration of multiple heat transfer mechanisms in cracked media. Second, while our current phase-field model shows good agreement with experimental results for basic mechanical parameters, we aim to develop more sophisticated constitutive models by incorporating: (1) porosity-dependent mechanical responses, (2) transitions between brittle and ductile behavior, and (3) complex damage evolution mechanisms. These enhancements will enable more accurate predictions of both thermal-mechanical coupling effects and mechanical performance of sintered silver across different porosity levels and loading conditions.

The Abaqus subroutine implementation of this work will be made publicly available. The implementation details and related materials can be obtained by contacting `yanpenggong@gmail.com`.

CRediT authorship contribution statement

Yanpeng Gong: Writing – original draft, Software, Project administration, Methodology, Funding acquisition, Formal analysis, Conceptualization. **Yuguo Kou:** Writing – review & editing, Visualization, Validation. **Qiang Yue:** Writing – review & editing, Supervision. **Xiaoying Zhuang:** Writing – review & editing, Supervision, Funding acquisition. **Navid Valizadeh:** Writing – review & editing. **Fei Qin:** Writing – review & editing, Supervision. **Qiao Wang:** Writing – review & editing. **Timon Rabczuk:** Writing – review & editing, Supervision.

Declaration of competing interest

The authors declare that they have no known competing financial interests or personal relationships that could have appeared to influence the work reported in this paper.

Acknowledgments

The authors acknowledge the support from the National Natural Science Foundation of China (No. 12002009) and the Alexander von Humboldt Foundation, Germany.

Data availability

Data will be made available on request.

References

[1] Long X, Guo Y, Su Y, Siow KS, Chen C. Constitutive, creep, and fatigue behavior of sintered Ag for finite element simulation of mechanical reliability: a critical review. J Mater Sci, Mater Electron 2022;1–17.

[2] Lee C-C, Kuo K-S, Wang C-W, Chang J-Y, Han W-K, Chang T-C. Packaging reliability estimation of high-power device modules by utilizing silver sintering technology. Microelectron Reliab 2020;114:113890.

[3] Yu F, Cui J, Zhou Z, Fang K, Johnson RW, Hamilton MC. Reliability of Ag sintering for power semiconductor die attach in high-temperature applications. IEEE Trans Power Electron 2016;32(9):7083–95.

[4] Blank T, Bruns M, Kuebel C, Leyrer B, Meisser M, Weber M, Rudzki J, Osterwald F, Wilke K, Busche N, et al. Low temperature silver sinter processes on ENIG surfaces. In: CIPS 2016; 9th international conference on integrated power electronics systems. VDE; 2016, p. 1–6.

[5] Feng J, Mei Y, Li X, Lu G-Q. Characterizations of a proposed 3300-V press-pack IGBT module using nanosilver paste for high-voltage applications. IEEE J Emerg Sel Top Power Electron 2018;6(4):2245–53.

[6] Wang Y, Li J, Agyakwa P, Johnson CM, Li S. Quantitative microstructure characterization of Ag nanoparticle sintered joints for power die attachment. Mol Cryst Liq Cryst 2014;604(1):11–26.

[7] Fan J, Xu D, Zhang H, Qian C, Fan X, Zhang G. Experimental investigation on the sintering kinetics of nanosilver particles used in high-power electronic packaging. IEEE Trans Compon Packag Manuf Technol 2020;10(7):1101–9.

[8] Hong WS, Kim MS, Oh C, Joo Y, Kim Y, Hong K-K. Pressureless silver sintering of silicon-carbide power modules for electric vehicles. Jom 2020;72:889–97.

[9] Long X, Hu B, Feng Y, Chang C, Li M. Correlation of microstructure and constitutive behaviour of sintered silver particles via nanoindentation. Int J Mech Sci 2019;161:105020.

[10] Herboth T, Guenther M, Fix A, Wilde J. Failure mechanisms of sintered silver interconnections for power electronic applications. In: 2013 IEEE 63rd electronic components and technology conference. IEEE; 2013, p. 1621–7.

[11] Yu D-j, Chen X, Chen G, Lu G-q, Wang Z-q. Applying anand model to low-temperature sintered nanoscale silver paste chip attachment. Mater Des 2009;30(10):4574–9.

[12] Kraft S, Zischler S, Tham N, Schletz A. B3. 3-properties of a novel silver sintering die attach material for high temperature-high lifetime applications. In: Proceedings SENSOR 2013. 2013, p. 242–7.

[13] Caccuri V, Milhet X, Gadaud P, Bertheau D, Gerland M. Mechanical properties of sintered ag as a new material for die bonding: influence of the density. J Electron Mater 2014;43:4510–4.

[14] Milhet X, Gadaud P, Caccuri V, Bertheau D, Mellier D, Gerland M. Influence of the porous microstructure on the elastic properties of sintered ag paste as replacement material for die attachment. J Electron Mater 2015;44:3948–56.

[15] Fu S, Mei Y, Li X, Ning P, Lu G-Q. Parametric study on pressureless sintering of nanosilver paste to bond large-area ($\geqslant$ 100 mm ^{2}) power chips at low temperatures for electronic packaging. J Electron Mater 2015;44:3973–84.

[16] Knoerr M, Schletz A. Power semiconductor joining through sintering of silver nanoparticles: Evaluation of influence of parameters time, temperature and pressure on density, strength and reliability. In: 2010 6th international conference on integrated power electronics systems. IEEE; 2010, p. 1–6.

[17] Li X, Chen G, Chen X, Lu G-Q, Wang L, Mei Y-H. High temperature ratcheting behavior of nano-silver paste sintered lap shear joint under cyclic shear force. Microelectron Reliab 2013;53(1):174–81.

[18] Zhao S, Dai Y, Qin F, Li Y, Liu L, Zan Z, An T, Chen P, Gong Y, Wang Y. On mode II fracture toughness of sintered silver based on end-notch flexure (ENF) test considering various sintering parameters. Mater Sci Eng: A 2021;823:141729.

[19] Carr J, Milhet X, Gadaud P, Boyer SA, Thompson GE, Lee P. Quantitative characterization of porosity and determination of elastic modulus for sintered micro-silver joints. J Mater Process Technol 2015;225:19–23.

[20] Chen Z, Wang X, Giuliani F, Atkinson A. Microstructural characteristics and elastic modulus of porous solids. Acta Mater 2015;89:268–77.

[21] Yao Y, Huang Q, Wang S. Effects of porosity and pore microstructure on the mechanical behavior of nanoporous silver. Mater Today Commun 2020;24:101236.

[22] Su Y, Fu G, Liu C, Zhang K, Zhao L, Liu C, Liu A, Song J. Thermo-elasto-plastic phase-field modelling of mechanical behaviours of sintered nano-silver with randomly distributed micro-pores. Comput Methods Appl Mech Engrg 2021;378:113729.

[23] Long X, Chong K, Su Y, Du L, Zhang G. Connecting the macroscopic and mesoscopic properties of sintered silver nanoparticles by crystal plasticity finite element method. Eng Fract Mech 2023;281:109137.

[24] Pillai U, Heider Y, Markert B. A diffusive dynamic brittle fracture model for heterogeneous solids and porous materials with implementation using a user-element subroutine. Comput Mater Sci 2018;153:36–47.

[25] Dittmann M, Aldakheel F, Schulte J, Schmidt F, Krüger M, Wriggers P, Hesch C. Phase-field modeling of porous-ductile fracture in non-linear thermo-elasto-plastic solids. Comput Methods Appl Mech Engrg 2020;361:112730.

[26] Yang Z-J, Li B-B, Wu J-Y. X-ray computed tomography images based phase-field modeling of mesoscopic failure in concrete. Eng Fract Mech 2019;208:151–70.

[27] Yue Q, Wang Q, Tian W, Rabczuk T, Zhou W, Ma G, Zhuang X, Chang X. A phase-field lattice model (PFLM) for fracture problem: Theory and application in composite materials. Compos Struct 2023;323:117432.

[28] Yue Q, Wang Q, Zhou W, Rabczuk T, Zhuang X, Liu B, Chang X. An efficient adaptive length scale insensitive phase-field model for three-dimensional fracture of solids using trilinear multi-node elements. Int J Mech Sci 2023;253:108351.

[29] Yue Q, Zhou W, Wang Q, Feng Y, Ma G, Chang X. An adaptive phase-field model based on bilinear elements for tensile-compressive-shear fracture. Comput Math Appl 2022;105:112–35.

[30] Wang Q, Yue Q, Zhou W, Feng Y, Chang X. Modeling of both tensional-shear and compressive-shear fractures by a unified phase-field model. Appl Math Model 2023;117:162–96.

[31] Emdadi A, Fahrenholtz WG, Hilmas GE, Zaeem MA. A modified phase-field model for quantitative simulation of crack propagation in single-phase and multi-phase materials. Eng Fract Mech 2018;200:339–54.

[32] Miehe C, Welschinger F, Hofacker M. A phase field model of electromechanical fracture. J Mech Phys Solids 2010;58(10):1716–40.

[33] Natarajan S, Annabattula RK, Martínez-Pañeda E, et al. Phase field modelling of crack propagation in functionally graded materials. Compos B: Eng 2019;169:239–48.

[34] Fang J, Wu C, Rabczuk T, Wu C, Ma C, Sun G, Li Q. Phase field fracture in elasto-plastic solids: Abaqus implementation and case studies. Theor Appl Fract Mech 2019;103:102252.

[35] Gong Y, Kou Y, Yue Q, Zhuang X, Qin F, Wang Q, Rabczuk T. The application of thermomechanically coupled phase-field models in electronic packaging interconnect structures. Int Commun Heat Mass Transfer 2024;159:108033.

[36] Badnava H, Msekh MA, Etemadi E, Rabczuk T. An h-adaptive thermo-mechanical phase field model for fracture. Finite Elem Anal Des 2018;138:31–47.

[37] Wang T, Ye X, Liu Z, Liu X, Chu D, Zhuang Z. A phase-field model of thermo-elastic coupled brittle fracture with explicit time integration. Comput Mech 2020;65:1305–21.

[38] Miehe C, Hofacker M, Schänzel L-M, Aldakheel F. Phase field modeling of fracture in multi-physics problems. Part II. Coupled brittle-to-ductile failure criteria and crack propagation in thermo-elastic–plastic solids. Comput Methods Appl Mech Engrg 2015;294:486–522.

[39] Zhou S, Zhuang X, Rabczuk T. Phase-field modeling of fluid-driven dynamic cracking in porous media. Comput Methods Appl Mech Engrg 2019;350:169–98.

[40] Goswami S, Anitescu C, Chakraborty S, Rabczuk T. Transfer learning enhanced physics informed neural network for phase-field modeling of fracture. Theor Appl Fract Mech 2020;106:102447.

[41] Wu J-Y. A unified phase-field theory for the mechanics of damage and quasi-brittle failure. J Mech Phys Solids 2017;103:72–99.

[42] Wang Q, Feng Y, Zhou W, Cheng Y, Ma G. A phase-field model for mixed-mode fracture based on a unified tensile fracture criterion. Comput Methods Appl Mech Engrg 2020;370:113270.

[43] Yue Q, Wang Q, Rabczuk T, Zhou W, Zhuang X, Chang X. A thermo-mechanical phase-field model for mixed-mode fracture and its application in rock-like materials. Int J Rock Mech Min Sci 2024;183:105907.

[44] Zhang Z, Eckert J. Unified tensile fracture criterion. Phys Rev Lett 2005;94(9):094301.

[45] Svolos L, Bronkhorst CA, Waisman H. Thermal-conductivity degradation across cracks in coupled thermo-mechanical systems modeled by the phase-field fracture method. J Mech Phys Solids 2020;137:103861.

[46] Dittmann M, Krüger M, Schmidt F, Schuß S, Hesch C. Variational modeling of thermomechanical fracture and anisotropic frictional mortar contact problems with adhesion. Comput Mech 2019;63:571–91.

[47] Wereszczak AA, Vuono DJ, Wang H, Ferber MK, Liang Z. Properties of bulk sintered silver as a function of porosity. 2012.

[48] Gadaud P, Caccuri V, Bertheau D, Carr J, Milhet X. Ageing sintered silver: relationship between tensile behavior, mechanical properties and the nanoporous structure evolution. Mater Sci Eng: A 2016;669:379–86.

[49] Russel A. Factors affecting the interlaminar fracture energy of graphite/epoxy laminates. In: Proc. 4th int. conf. comp. mater.. 1982, p. 279–86.